Small size of recorded neuronal structures confines the accuracy in direct axonal voltage measurements

Viktor János Oláh[1,2], Gergely Tarcsay[1] and János Brunner[1]

[1] Laboratory of Cellular Neuropharmacology, Institute of Experimental Medicine, Budapest, Hungary

[2] János Szentágothai School of Neurosciences, Semmelweis University, Budapest, Hungary

Corresponding Author: János Brunner

Email: brunner.janos@koki.hu

Abstract

Patch-clamp instruments including amplifier circuits and pipettes affect the recorded voltage signals. We hypothesized that realistic and complete *in silico* representation of recording instruments together with detailed morphology and biophysics of small recorded structures will precisely reveal signal distortions and provides a tool that predicts native signals from distorted voltage recordings. Therefore, we built a model that was verified by small axonal recordings. The model accurately recreated actual action potential measurements with typical recording artefacts and predicted the native electrical behavior. The simulations verified that recording instruments substantially filter voltage recordings. Moreover, we revealed that instrumentation directly interferes with local signal generation depending on the size of the recorded structures, which complicates the interpretation of recordings from smaller structures, such as axons. However, our model offers a straightforward approach that predicts the native waveforms of fast voltage signals and the underlying conductances even from the smallest neuronal structures.

1

23

Introduction

Patch-clamp technique is affected by limitations that originate primarily from the physical properties of the recording pipettes (Benndorf, 1995; Hamill, Marty, Neher, Sakmann, & Sigworth, 1981; Marty & Neher, 1995). Patch pipettes have significant resistance (R_{pip}) and their glass wall represent a substantial capacitive surface (C_{pip}) as well. Limitations can be reduced by optimizing the recording conditions (that is, with the reduction of the R_{pip} and C_{pip}) and corrected by using compensatory mechanisms of the amplifiers. Under standard recording conditions in measurements from relatively large structures, such as neuronal somata, these optimizations and corrections can sufficiently reduce distortions to an acceptable level. Therefore, the difference between the recorded and native voltage signals are negligible during good current clamp conditions in most neuronal structures. However, the reduction of instrumental distortions could became inherently insufficient in cases where the recorded structures are small, such as most of the central synapses. Recording pipettes for small neuronal structures must have small tip, which inevitably results in larger R_{pip} values that substantial filters the recorded signals (Benndorf, 1995; Novak et al., 2013; Ying, Bruckbauer, Rothery, Korchev, & Klenerman, 2002). Consequently, the fast voltage signals such as the action potentials (APs) are particularly vulnerable to signal distortion associated with direct recordings in small axonal structures. The shape of axonal APs is a key determinant of neuronal signaling that affects neurotransmitter release and short-term dynamics in synaptic connections (Bean, 2007; Borst & Sakmann, 1999; Chao & Yang, 2019; Geiger & Jonas, 2000; Katz & Miledi, 1967; Kawaguchi & Sakaba, 2015; Zbili & Debanne, 2019). Therefore, accurate AP measurements are essential to understand fundamental mechanisms of the neuronal information flow. Recent developments of the recording apparatus allows collecting voltage signals from the finest axonal structures (Kawaguchi & Sakaba, 2015; Novak et al., 2013; Ritzau-Jost et al., 2021; Rowan, DelCanto, Jianqing, Kamasawa, & Christie, 2016; Vivekananda et al., 2017). However, the interpretation of these signals are still limited because signal distortions caused by the recording pipette and amplifier circuits remains elusive (Ritzau-Jost et al., 2021). We reasoned that as computational modeling allows the precise reconstruction of the native electrical behavior of the most complex

2

48   neuronal structures (Henrik Alle, Roth, & Geiger, 2009; Beaulieu-Laroche & Harnett, 2018; Branco & Häusser,

49   2011; Jayant et al., 2017; Kwon, Sakamoto, Peterka, & Yuste, 2017) it should be similarly possible to simulate

50   the behavior of the recording instruments.

51   With these in mind, we built and tested a realistic model that considers not only the biological structures but also

52   amplifier and pipette features. With this complex model we simulated actual recording conditions with the aim

53   of subsequent, simulated removal of the instrumental contributions and distortions from the recorded signals.

54   Thus, this complex model allowed the correction of the distortions caused by patch-clamp recording instruments

55   and predict isolated biological signals. We tested the model by predicting the native action potential waveform of

56   a directly recorded small axonal varicosity. Our simulations showed that recording instrumentation not only filters

57   the signal, but it directly interferes with native signal generation in small neuronal structures.

58

Results

60   *In silico implementation of amplifier features*

61   We developed and validated a realistic amplifier model working both in voltage clamp (VC) and current clamp

62   (CC) mode using the NEURON simulation environment (Hines & Carnevale, 1997). The model needed to be

63   suitable for both VC and CC modes, because instrumental compensations are typically determined in VC mode

64   during seal formations and these settings are implemented for CC during voltage signals recordings. For precise

65   implementation of the components of the amplifier circuit, we examined their capacitive and resistive properties

66   using three test configurations (**Supplementary Figure 1**). The first test configuration was the isolated headstage

67   in open circuit (test #1), which allowed the characterization of the high frequency boost unit (see below) and the

68   capacitance compensation of the VC circuitry. Since open circuit measurements are not possible in CC mode, the

69   circuit was closed via known resistors in the second test configuration (test #2). This configuration allowed the

70   estimation of stray capacitance associated with the feedback resistor. The third test circuit was a modified model

71   cell (test #3, type 1U, Molecular Devices), which represents whole-cell recording conditions as it includes an

72 idealized cell and recording pipette with their resistive and capacitive components. In order to explore an extended

73 range of signal processing capacity of the amplifier, model cell components were varied using custom capacitors

74 and resistors. This test configuration allowed us to investigate the features of the capacitance neutralization of the

75 CC circuitry.

76 The construction of our model amplifier initially based on idealized circuit representations, namely a resistive

77 feedback circuit (a current-to-voltage converter) typical for the VC and a voltage follower circuit (a unity gain

78 voltage buffer) with an idealized current source for the CC (Sherman-Gold, 2012; Sigworth, 1995; Wilson &

79 Park, 1989) (**Figure 1**).

80
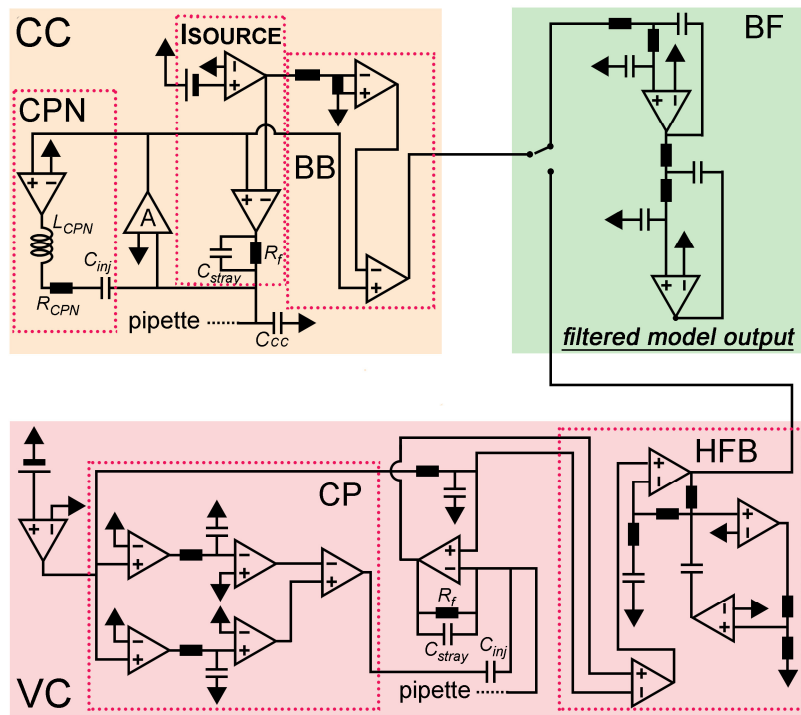
81 **Figure 1. Model amplifier**

82 Schematic circuit diagram of the model amplifier. The current clamp circuit (CC) consisted of a current source (ISOURCE),

83 an idealized voltage buffer (A), capacitance neutralization (CPN) and bridge balance (BB) circuits. The voltage clamp

84 circuit (VC) consisted of a resistive feedback amplifier with dual capacitance compensation (CP) and the high frequency

85 boost circuit (HFB). Outputs of the two amplifier modules are connected to a low-pass filter circuit (BF).

86

87   Operation of combined voltage- and current-clamp amplifiers requires a capacitor (C_{inj}) for current injection in

88   both VC and CC modes and a resistor (R_f) used as current generator in CC and as feedback resistor in VC

89   (Strickholm, 1995) (**Figure 1**). To create realistic amplifier model, we first measured amplifier responses using

90   the three test circuits, which were subsequently simulated allowing individual tuning of elementary circuit

91   parameters. First, we measured C_{inj}, assuming that the total capacitive load present in the isolated VC circuit (test

92   #1) corresponds to the injector capacitor. By recording voltage-step-evoked capacitive current responses in open

93   circuit configuration, we determined that the total capacitive load is 1.615 pF in our amplifier (MultiClamp700B).

94   As virtually all real resistors, R_f has a certain amount of parasitic capacitance (C_{stray}) which affects the

95   performance characteristics of the amplifier. We next determined the size of this parasitic capacitance. In CC

96   mode, the C_{stray} connected in parallel with the R_f (see ISOURCE circuit on **Figure 1**) acts as a capacitance-

97   neutralizing element. However, this neutralizing effect appears only when the input load is considerably smaller

98   than the R_f which was set to 500 MΩ in the real amplifier (**Figure 2A left traces**). To characterize the size of

99   C_{stray} associated with the R_f, we adjusted the C_{stray} in the model to reproduce the evoked voltage responses recorded

100   with the amplifier in test #2 configuration with 20, 50 and 100 MΩ input loads (**Figure 2A right traces**). These

101   simulations revealed 0.38 pF C_{stray}, thus we used this value in the model.

102   Next, we added the remaining amplifier components to the model one-by-one. First, we focused on the VC

103   operations whose speed depends on a dedicated high frequency boost circuit (Sigworth, 1995). Amplifier are built

104   with this compensation mechanism because C_{stray} substantially reduces the output bandwidth of the feedback

105   circuit in VC mode (time constant of the capacitive relaxation with the previously determined 0.38 pF C_{stray}:

106   191.92 μs, **Figure 2B left**). We added a simplified boosting unit tuned to accelerate model responses to the

107   experimentally observed amplifier speed (3.85 μs vs. 3.19 μs, real vs. boosted model, **Figures 1 and 2B right**).

108   Next, we implemented two pipette capacitance compensation circuits in the VC model. Fast capacitance

109   compensation (CPf, 0-16 pF, 0.5-1.8 μs) cancels the majority of C_{pip}-induced current transients, while the slow

110   capacitance compensation (CPs, 0-3 pF, 10-4000 μs) reduces the slower instrumental capacitive components

111 (Sigworth, 1995) (not equivalent to whole-cell compensation that was not implemented in this model **Figures 1**

112 **and 2C**).
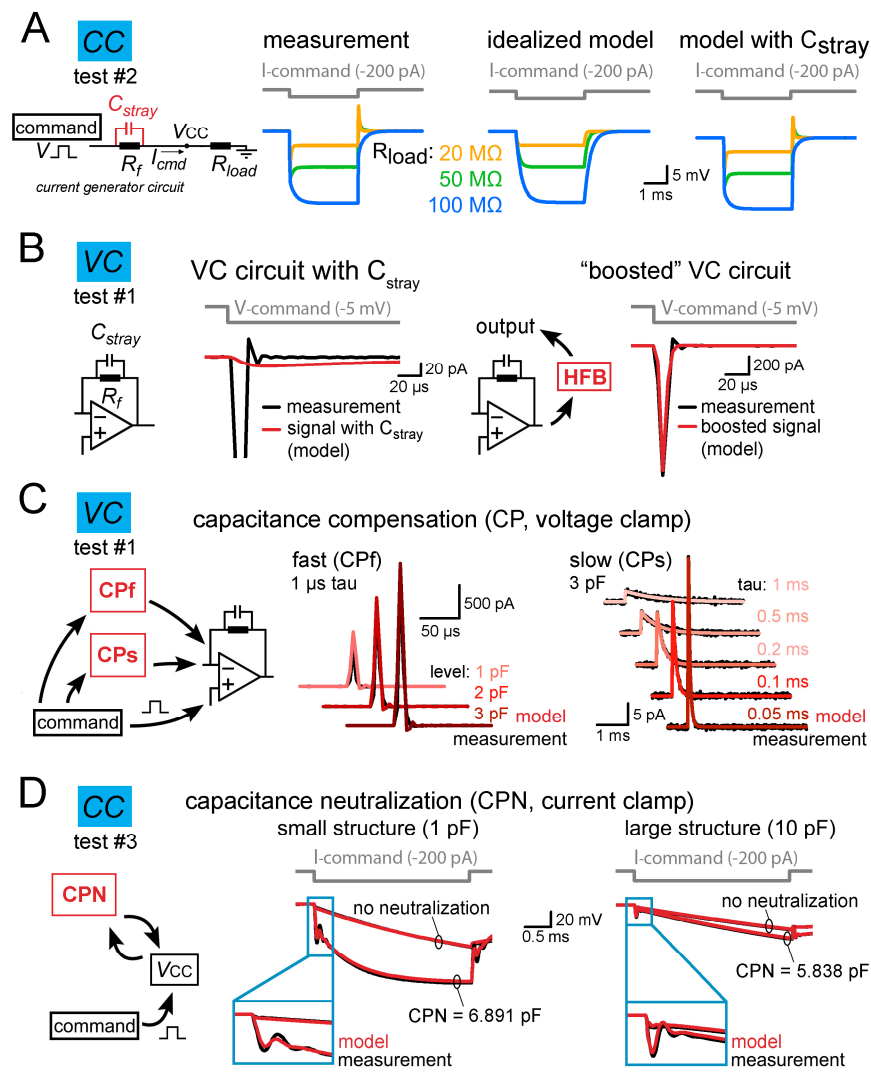
Figure 2. Implementation of individual amplifier components with realistic parameters

(A) The stray capacitance (C_{stray}) associated with the current passing resistor (R_f) was predicted by simulating the voltage responses recorded in test #2 configuration. C_{stray} acts as a capacitance neutralizing element in CC mode. Because the capacitance neutralizing effect of C_{stray} depends on the load resistance (R_{load}) attached to the amplifier input (V_{CC}), we tested three scenarios using 20, 50 and 100 MΩ resistors. The left traces show measured voltage responses evoked by brief current injection in the presence of different R_{load}. Idealized (i.e. C_{stray} free) model responses are shown in the middle for comparison. Right, model responses with 0.38 pF C_{stray} replicated the observed amplifier behavior.

(B) C_{stray} of R_f slows down the current responses in the VC model (red trace, left panel). This effect is compensated in the actual amplifiers by using high frequency boost circuit (HFB). The implementation of a high frequency boost circuit in the model restored the response speed (red trace, right panel).

6

(C) Capacitance compensation in the VC model (red) faithfully replicates the magnitude and the time course of amplifier-generated compensatory currents (black, test circuit#1) for both the fast (CPf) and slow (CPs) compensations.

(D) Comparison of simulated (red) and recorded (black) voltage signals obtained with different capacitance neutralization (CPN) in CC mode from a small structure (middle panel) and from a large structure (left panel). Notice that the instrumental CC model faithfully replicates the neutralizing capability of the amplifier and the neutralization associated signal artefacts regardless of the applied CPN settings.

We also implemented two compensatory mechanisms for the CC mode, namely the capacitance neutralization (CPN) and the bridge balance (BB) compensation (**Figure 1**). The CPN circuit is a positive feedback loop that feeds the pipette voltage back to the input through the C_{inj} in order to discharge the pipette capacitance (Sherman-Gold, 2012; Wilson & Park, 1989). Due to this positive feedback, the recordings are prone to oscillate as CPN level approaches a fully compensated state. Such evolving oscillation carry information about the intrinsic behavior of the CPN circuit. Therefore, the oscillating signal (dampening and frequency profile) can be employed for determining a minimal set of passive circuit elements necessary the re-create the CPN behavior. Specifically, we measured the maximal possible capacitance neutralization where the recording is still stable using test#3 circuit. Pipette parameters (10MΩ, 2.8 pF) and the cell-equivalent resistor (500 MΩ) was fixed and only the capacitance of the cell was varied from 0.75 pF to 46.7 pF. The model reproduced the recorded signal artefacts when a resistor (1.49 MΩ) and an inductor (18.3 H) was incorporated to the CPN circuit in series with the C_{inj} (**Figures 1 and 2D**). Amplifiers are typically supplied with BB compensatory mechanism to eliminate the voltage drop across the access resistance (Araki & Otani, 1955; Sherman-Gold, 2012). In the model, we subtracted a scaled version of the command signal from the recorded voltage (**Figure 1**). We also extended our model with a four-pole low-pass Bessel filter unit with adjustable cutoff frequencies from 0.5 kHz to 100 kHz (**Figure 1**).

Altogether, by using a measurement-based approach we created an amplifier model, in which both the VC and CC operation and their specific compensatory capabilities show realistic behavior.

150 *Pipette implementation considers the observed nonuniform C_{pip} and R_{pip} distributions*

151 Next, we focused on the accurate implementation of patch pipettes. To properly characterize the distribution of

152 resistance along patch pipettes that are suitable for recordings from small axons, we repeatedly broke small pieces

153 from the end of the pipettes and determined the resistance as a function of tip distance (**Figure 3A**, n = 55

154 resistance measurement). In agreement with the theoretical considerations (Benndorf, 1995; Ying et al., 2002),

155 we found that pipette resistance drops sharply after the tip, falling below one MΩ within the first millimeter (0.33

156 ± 0.18 MΩ for measurements with tip distance over 1 mm, n=20 measurement). To determine the capacitance

157 distribution of our pipettes we systematically varied the immersed length of the pipettes in the recording solution

158 and measured the capacitance, which corresponds to the cumulative capacitance of the dipped part (Cornwall &

159 Thomas, 1981) (**Figure 3A**, n = 656 capacitance measurement). The cumulative capacitance increased within the

160 first 3 mm from the tip, whereas the remaining part of the pipette had only moderate contribution to the total

161 capacitance suggesting inhomogeneous capacitance distribution along pipettes (0.03 ± 0.07 pF, 2.52 ± 0.3 pF and

162 3.1 ± 0.25 pF at 0.1 mm, 3 mm and 7 mm tip distances respectively, n=39, 40 and 38 measurements, **Figure 3A**).

163 A key parameter that defines the pipette capacitance is the ratio of the outer and inner pipette diameters (R_{OI})

164 (Benndorf, 1995; Cornwall & Thomas, 1981). One potential explanation for the inhomogeneous capacitance

165 distribution is that the R_{OI} is not constant along the pipette but it decreases toward the tip. To test this possibility

166 and verify the predictions of the capacitance distribution measurement, we directly measured the R_{OI} of the

167 recording pipettes. In order to precisely measure the edge of the pipette walls and avoid optical distortions by the

168 curved glass walls, we carefully split the pipettes using a custom-built grinding system and measured their inner

169 and outer diameters along the longitudinal axis (**Figure 3B**, see Methods section for details). Consistent with the

170 dipping measurements, R_{OI} decreased toward the tip (R_{OI} <2mm = 1.6 ± 0.02 vs. R_{OI} >5mm = 2.04 ± 0.02, n = 4

171 pipettes) explaining the larger contribution of the tip region to the total pipette capacitance.
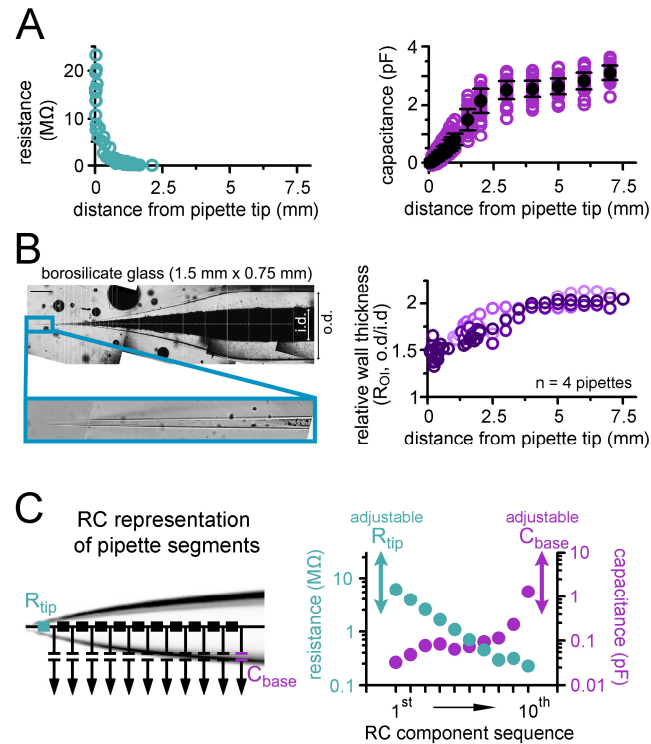
Figure 3. Implementation of pipettes with non-uniform C_{pip} and R_{pip} distributions

(A) Pooled data of R_{pip} (left graph) and C_{pip} (right graph) as a function of tip distance.

(B) A representative imaging plane that was used for the measurement of the relative wall-thickness (R_{oi}) that is, the ratio of outer and inner diameter (o.d. and i.d., respectively) of the pipettes. Scale bar: 0.5 mm. Graph on the right shows that the wall of the pipettes is much thinner toward the tips (i.e. the inner diameter is larger than predicted from the R_{oi} of the original glass; the 4 measured pipettes are shown in different shades of purple).

(C) Pipettes were implemented as 10 independent RC units, a resistor (R_{tip}, on the left) and a capacitor (C_{base}, on the right). The two latter components allow the adjustment of the model to fit the differences of R_{pip} and C_{pip} of individual pipettes. Graph on the right indicates the actual capacitance (purple) and resistance (green) values of the 10 fixed RC motifs.

Based on these measurements, we created the skeleton of a "prototypical" patch pipette model from 10 RC units to consider the inhomogeneous distribution of capacitance and resistance (**Figure 3C**). Model pipette parameters can be adjusted to account for variability across individual pipettes using an additional resistor placed to the tip and a capacitor placed to the back to tune the R_{pip} and C_{pip} of individual pipettes.

9

188   *Reconstitution of the native electrical behaviour of a small axon*

189   To test the efficacy of the complex instrumental model in predicting undisturbed fast neuronal membrane

190   responses from distorted recordings, we used patch-clamp data from a small (<1 µm) *en passant* axonal varicosity

191   of an identified hippocampal mossy fiber axon (MF, **Figure 4A**). Recordings from submicron-sized neuronal

192   structures are supposedly substantially distorted as they can be patched only with high access resistance and their

193   capacitance is in the range of the remaining uncompensated instrumental capacitance.

194   The experimental conditions needed to be realistically modeled, including the precise morphology and electrical

195   properties of the biological structure and the instrumental conditions (**Supplementary Figure 2**, see Methods for

196   details). First, we characterized the total instrumental capacitance (C_{tot}, the sum of all amplifier-, holder- and

197   pipette-related capacitances) present in the actual recording (**Figure 4A**, C_{tot} : 7.097 pF from which 3.23 pF is the

198   C_{pip} and 2 pF is the capacitance of the pipette holder). Target trace for this estimation was recorded using both

199   fast and slow pipette capacitance compensation of the amplifier with the highest frequency resolution (output

200   filter was bypassed) and we set the model accordingly.

201   Next, we precisely reconstructed the morphology of the biocytin-labelled and fluorescently recovered MF axon

202   because signal propagation strongly depends on the length, diameter and their inhomogeneties of the biological

203   structures (Goldstein & Rall, 1974; Manor, Koch, & Segev, 1991) (**Figure 4B**). As it is characteristic for

204   hippocampal mossy fibers the 519 µm long reconstruction of the recorded MF included large (>3 µm) terminals,

205   filopodial extensions and small (<1.5 µm) *en passant* varicosities within the *stratum lucidum* of the CA3 area

206   (Acsady, Kamondi, Sık, Freund, & Buzsáki, 1998; Rollenhagen et al., 2007).

207   We next determined the cable properties; specific membrane resistance (R_m), membrane capacitance (C_m), and

208   intracellular resistivity (R_i) of the particular axon. For this, we optimized the model to the experimentally recorded

209   voltage responses evoked by short and long current stimuli (**Figure 4C**) (Nörenberg, Hu, Vida, Bartos, & Jonas,

210   2010; Roth & Häusser, 2001; Schmidt-Hieber, Jonas, & Bischofberger, 2007; Szoboszlay et al., 2016). The

211   advantages of the complex (instrumental + biological) model became obvious in these fittings. Pipette artefacts

212 can markedly contaminate the onset of the evoked responses upon current injection (Major, Larkman, Jonas,

213 Sakmann, & Jack, 1994). The incorporation of the complete experimental instrument to the model precisely

214 reproduced these stimulus artefacts, therefore, allowing us to isolate biological contributions and obtain the

215 passive cellular parameters. The predicted cellular parameters (R_m = 60.0 kΩ*cm^2, a C_m = 0.65 μF*cm^{-2} and R_i

216 = 147.3 Ω*cm) match with the data reported for MFs using recordings from large terminals (S. Hallermann,

217 Pawlu, Jonas, & Heckmann, 2003). It is important to note that the similarities of the simulated and recorded fast

218 voltage transients further verify our complex model.
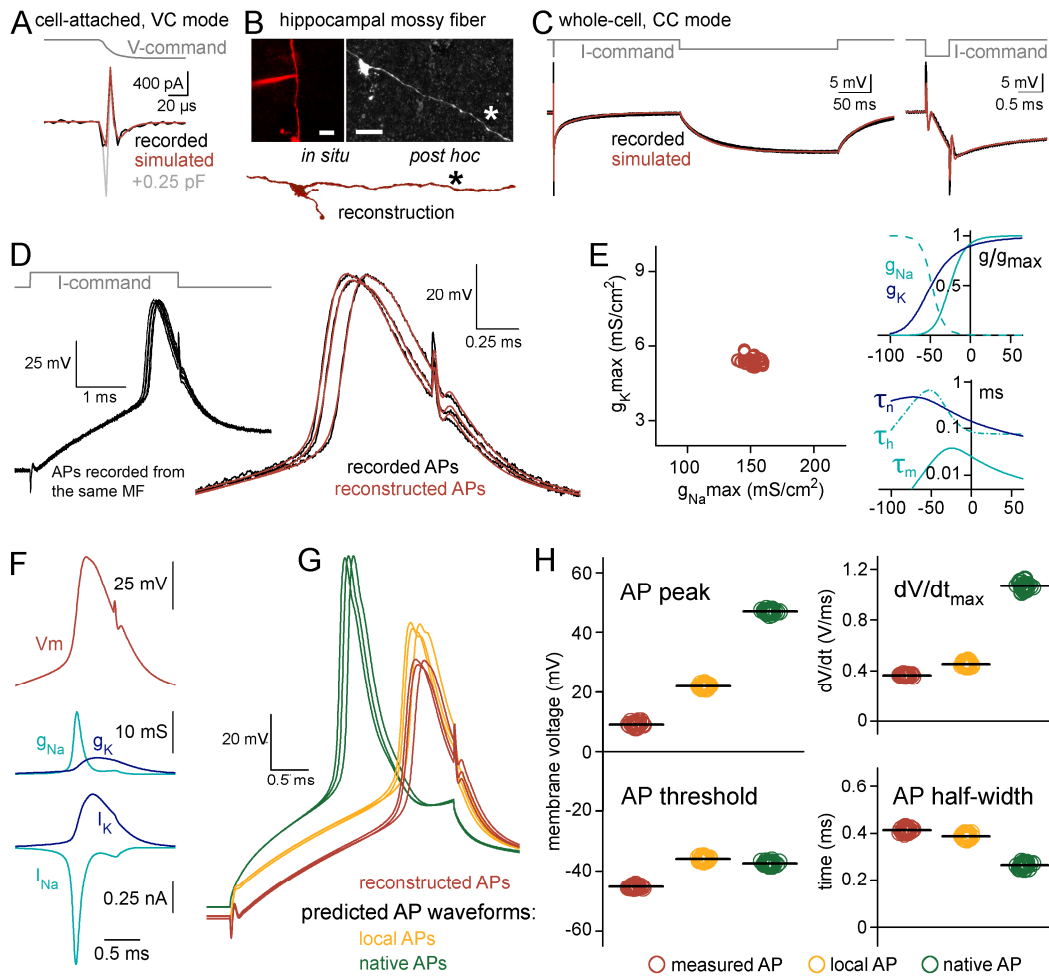
220 **Figure 4. Reconstitution of the undisturbed membrane dynamics of a recorded axon**

221 (A) Current responses to -20 mV voltage steps recorded from the axonal membrane in on-cell mode (black) and in the model

222 with 7.097 pF (red) and 7.347 pF (grey) C_{tot}. Notice the sensitivity of simulated responses to small differences in the

223 instrumental capacitance applied in the model.

(B) Confocal z-stack images show the recorded axon at the end of the experiment (left) and after the anatomical recovery (right). Bottom, part of the reconstructed morphology. Asterisks mark the recording position. Scale bars: 10 μm

(C) Voltage responses in the recorded axon (black) and in the passive cable model with the added instrument (red) to short (3 ms, −50 pA) and long (250 ms, −2.5 pA) current stimuli. The short pulse is shown at an expanded timescale on the right.

(D) Recorded (black) and simulated APs (red) evoked by brief (3 ms, 86 pA) current stimuli. APs were simulated in the complex model that included the instrument, the passive cable and Hodgkin-Huxley type sodium and potassium conductances.

(E) Left, distribution of optimal maximal Na^+ (gNa_{max}) and K^+ (gK_{max}) conductance densities obtained from 30 recorded and independently fitted APs. Right, averaged gating properties and voltage dependence of the conductances that were resulted in by the fits that recreated the recorded APs.

(F) Simulated AP waveform (top) with the underlying conductances (middle, g_{Na} and g_K) and the modeled ionic currents (bottom, I_{Na} and I_K).

(G) The simulations with the confirmed conductance sets allowed to see the waveforms of the same APs not only within the pipette (red, corresponding to measured APs) but also the simultaneous AP waveforms within the axon (orange, corresponding to local APs) and, after the removal of the recording instrument from the model, the native, undisturbed AP waveforms (green).

(H) Differences in waveform parameters of measured, local and native APs. Individual points show the peak, threshold, maximum rate of the rise (dV/dt_{max}) and half-width of 30 independently simulated APs in the three points of view. Horizontal black lines indicate mean values.

Next, we simulated the active ionic mechanisms underlying the recorded AP waveforms. APs were evoked with brief current stimuli (**Figure 4D and E**, 3 ms, 86 pA). To simulate APs we tuned Hodgkin-Huxley-type sodium and potassium conductances (Hodgkin & Huxley, 1952) (modified version of the built-in mechanism in the NEURON simulation environment). Optimization of the density, kinetics and voltage dependence resulted in AP waveforms closely matching to the recorded ones (absolute AP peak: 9.0 ± 0.12 mV vs. 9.28 ± 0.12 mV, recorded vs. simulated APs, respectively, AP half-width: 0.52 ± 0.002 ms vs. 0.52 ± 0.002 ms,, AP threshold: -45.28 ± 0.07 mV vs. -44.27 ± 0.16 mV, maximum rate of rise: 363.26 ± 0.93 vs. 432.27 ± 3.56, n = 30 APs; **Figure 4D**). This suggest that the complex instrumental model in combination with traditional conductance functions is sufficient to reconstruct the recorded AP waveforms from potentially distorted recordings. Importantly, although

12

253 each of the target APs was fitted independently, the optimal model conductance parameters were confined to a

254 narrow range within the parameter space (coefficient of variation = 3% for both the Na^+ and K^+ conductance

255 predictions, maximal g_{Na} density: 151.7 ± 5.23 mS/cm^2, maximal g_K density: 5.41 ± 0.16 mS/cm^2, n = 30; **Figure**

256 **4E**) indicating that the optimization provided a unique solution for the experimental data. Analysis of the error

257 between the fit and its target data in different Na^+ and K^+ conductance combinations also revealed a single

258 minimum that coincided with the best fit parameter combinations (**Supplementary Figure 3**). Furthermore, the

259 optimal conductance parameters (i.e. their maximal conductance levels, their voltage dependence, and their

260 activation and inactivation time constants), as well as the resulted ionic currents, are similar to previously

261 described mechanisms underlying cortical axonal APs at near-physiological temperature (Henrik Alle et al., 2009;

262 Geiger & Jonas, 2000; Stefan Hallermann, De Kock, Stuart, & Kole, 2012; Schmidt-Hieber & Bischofberger,

263 2010) (H. Alle, Kubota, & Geiger, 2011; Engel & Jonas, 2005; Hu & Jonas, 2014) (**Figure 4 E and F**), confirming

264 the validity of our AP-reconstitution approach.

265 The relatively high series resistance (R_{access}) in the recording (modeled R_{access}: 53.2 ± 1.02 MΩ in the AP

266 reconstitution simulations) can result in significant pipette filtering. The complex model, however, allowed us to

267 investigate not only the APs recorded through the pipette but also the local spike that occurred within the axon

268 while it was patched (**Figure 4G**). These local APs are not affected by the filtering effect caused by the pipette,

269 so we could directly quantify filtering effects by comparing the *local* and *recorded* axonal AP waveforms (**Figure**

270 **4H**). Because of the filtering, local spikes had larger peak amplitudes and faster time course than the recorded

271 APs (absolute peak: 21.95 ± 0.12 mV vs. 9.0 ± 0.12 mV, local vs. measured AP, respectively, *p = 6.88*10^{-60},*

272 *t(29) = -552.75 paired sample t-test*, n = 30 APs, half-width: 0.48 ± 0.002 ms vs. 0.52 ± 0.002 ms, local vs.

273 measured AP, respectively, *p = 1.99 * 10^{-17}, t(29) = 18.23, paired sample t-test*, n = 30 APs, **Figure 4H**). As

274 expected, the maximal rate of rise (dV/dt_{max}) during the upstroke of spikes was the most different between local

275 and measured APs as it is the most sensitive to low-pass filtering introduced by the pipette (453.11 ± 2.54 V/s vs.

276 363.26 ± 0.93 V/s, respectively, *p=4.69 * 10^{-29}, t(29) = -47.5, paired sample t-test*, n = 30 APs, **Figure 4H**).

277   Altogether, these observations are in agreement with the expected filtering, which affects fast signals, such as the

278   axonal APs more prominently.

279   Our model predicts that APs of the small MF bouton had lower peak and slower kinetics than APs measured from

280   large MF terminals (Henrik Alle et al., 2009; Geiger & Jonas, 2000). These observed differences could derive

281   either from biological variability among the subcellular compartments or from the larger deteriorating

282   instrumental impact on the local membrane of the smaller axon. To discriminate between these possibilities, we

283   investigated the *native* AP parameters predicted by the model. In this arrangement, we run the modeled biological

284   structure with the reconstructed model conductances but the recording instruments was removed (**Figure 4G and**

285   **H**). Thus, we predict how the native APs would look if the recording instrument was not present. We found that

286   the native APs reached more depolarized peak potential (46.9 ± 0.09 mV, *p = 2.27*10^{-48}, t(29) = 221.43, paired*

287   *sample t-test*, n = 30 APs) and were significantly faster (half-width: 0.33 ± 0.002 ms, *p = 1.36*10^{-33}, t(29) = -*

288   *68.3, paired sample t-test*; dV/dt$_{max}$: 1064.81 ± 5.1 V/s, *p = 3.75*10^{-45}, t(29) = 171.47, paired sample t-test*, n =

289   30 APs) compared to the local spikes modeled with the experimental rig. The obtained native AP parameters were

290   similar to those reported from large MF boutons, suggesting that the different AP shape observed in the small MF

291   recording is primarily attributable to the presence of the measuring system.

292   Altogether, these results show that it is possible to obtain the native and local AP properties and the plausible

293   underlying mechanisms using a complex instrumental model.

294

295   ***Modeling the recording instruments accurately predicts signal distortions and native AP shapes***

296   We used additional experiments to verify the reliability and plausibility of the model predictions. Specifically,

297   we recorded APs with three different capacitance neutralization settings from the same axon and tested whether

298   it alters the output of the model (CPN=6.5, 7 and 7.384 pF **Figure 5A**). Sub-optimal CPN conditions affects the

299   recorded signal in several ways (**Supplementary Figure 4**). The simulations reproduced the recorded APs with

300   different level of distortions when the CPN in the model was adjusted accordingly (**Figure 5A**). In addition, the

14

301 predicted underlying sodium and potassium conductances were also very similar (g_{Na} density: 159.02 ± 1.73

302 mS/cm^2, 151.7 ± 0.95 mS/cm^2, 160.03 ± 1.47 mS/cm^2, g_K density: 5.83 ± 0.05 mS/cm^2, 5.41 ± 0.03 mS/cm^2, 6.32

303 ± 0.09 mS/cm^2; n = 30, n = 30 and n = 28 for CPN = 6.5 pF APs, CPN = 7 pF APs and CPN = 7.386 pF APs,

304 respectively, **Figure 5B** and **Supplementary Figure 5**).
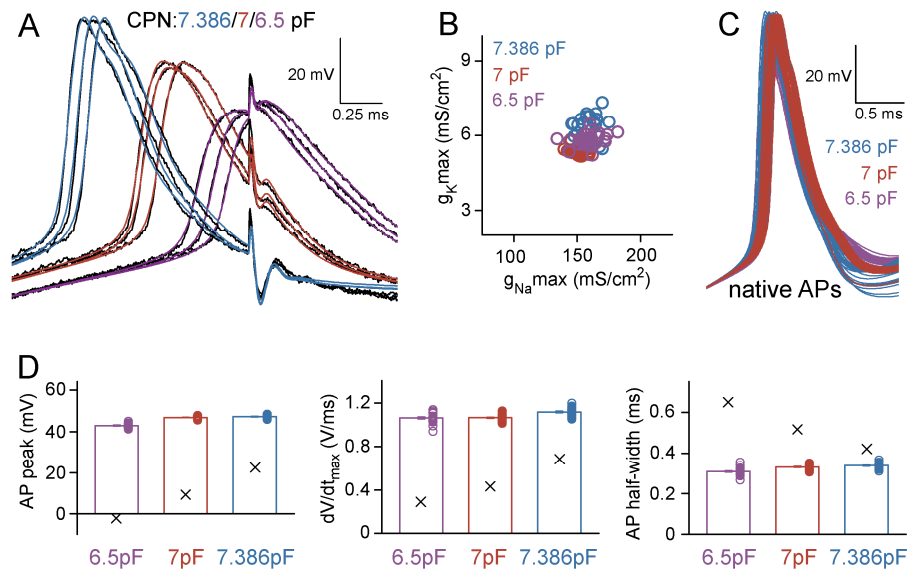
Figure 5. APs recorded and simulated from the same axon under different instrumental distortions predicted similar native spike shapes

(A) Representative target APs (black) and their best-fit representations in the complex instrument+axon model with standard CPN settings (red, 7 pF), with slightly reduced CPN (purple, 6.5 pF) or with the highest attainable CPN level (blue, 7.386 pF).

(B) The best-fit gNa_{max} and gK_{max} were similar from APs with different CPN levels (n=30, 30 and 28 target APs).

(C) The native AP waveforms retrieved from APs with different CPN levels were also similar.

(D) Peak, maximal dV/dt and half-width of the native APs predicted based on recordings with three different CPN settings. Columns show the averages of the native APs, while X denotes the averages of the experimentally measured parameters (n=30,30 and 28 APs) which were distorted by the instruments.

Importantly, not only the predicted AP shapes matched but the native APs were also similar despite of the different levels of distortions in the three independent original recording conditions (absolute AP peak: 43.0 ± 0.17 mV, 46.9 ± 0.09 mV, 47.2 ± 0.14 mV, AP half-width: 0.31 ± 0.003 ms, 0.33 ± 0.002 ms, 0.34 ± 0.003 ms; n=30, n=30,

15

320 n=28 for CPN=6.5 pF APs, CPN=7 pF APs and CPN=7.386 pF APs, respectively; **Figure 5C and D**). For an

321 additional verification, we tested whether the model provides consistent predictions of AP propagation across

322 conductance sets derived from different recording configurations. Specifically we simulated the natural AP

323 conduction of distally evoked APs to the original recording site (423 μm away, **Figure 6A**) and measured the

324 speed of propagation and the shape of the incoming APs. The incoming propagating APs were similar (absolute

325 AP peak: 61.73 ± 0.13 mV, 64.22 ± 0.07 mV, 65.48 ± 0.08 mV, AP width at -10 mV: 0.34 ± 0.003 ms, 0.36 ±

326 0.002 ms, 0.33 ± 0.002 ms; n=30, n=30, n=28 for CPN=6.5 pF APs, CPN=7 pF APs and CPN=7.386 pF APs,

327 respectively; **Figure 6**).
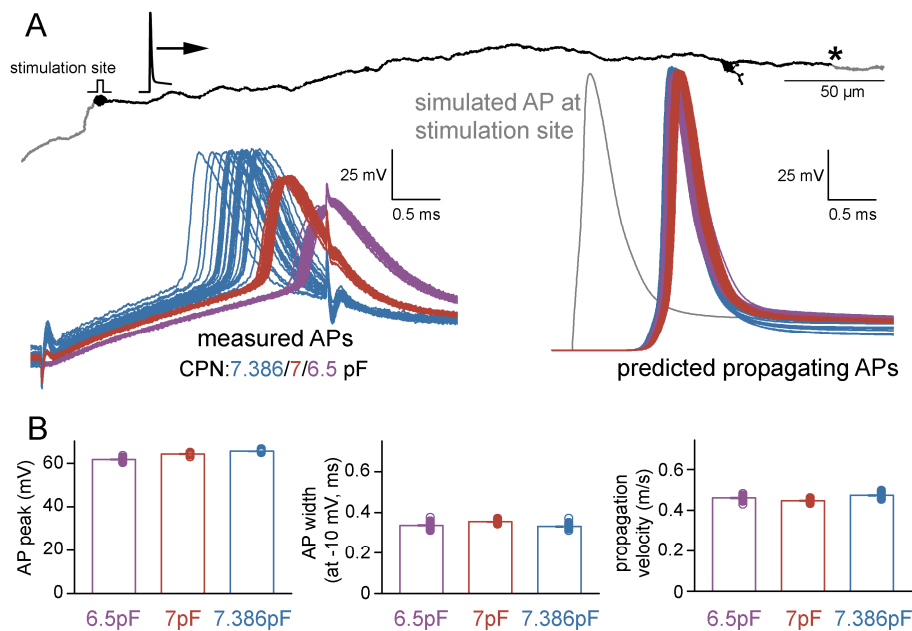
328

329 **Figure 6. Characteristics of propagating native APs**

330 (A) The reconstructed and simulated axonal structure with the position at which native AP parameters were captured

331 (indicated with asterisk) after distal AP initiation (stimulation site) in individual models that were optimized for different

332 recording conditions. Left, 88 original AP recordings that were used for the AP optimization in the models and recorded

333 individually with three different CPN settings (n=30, 30 and 28 with 6.5, 7 and 7.368 pF CPN, respectively). The retrieved

334 conductance sets were applied to the complete axon individually in all 88 cases. The right panel shows the 88 native,

335 propagating simulated APs at the indicated distal point along the axon. The color is as for the measured APs on the left. A

336 simulated AP at the stimulation site is shown in gray.

16

(B) Peak, width at -10 mV and propagation velocity of the distally initiated propagating APs retrieved from 88 individual simulations. Note that conventional AP half-width measurements can not be applied for propagating APs because of the altered apparent threshold.

The prediction of AP propagation velocity is particularly sensitive to model parametrization as the speed of axonal spike propagation strongly depends both on the morphological properties of the axon and the specific passive and active mechanisms of the axonal membrane. Consistent with previous measurements in hippocampal MFs (Henrik Alle et al., 2009; Kress, Dowling, Meeks, & Mennerick, 2008), all model configuration predicted similar propagation speed (0.46 ± 0.002 m*s^{-1}, 0.45 ± 0.001 m*s^{-1}, 0.47 ± 0.002 m*s^{-1}; **Figure 6B**).

Taken together, these results confirm that complete representation of the recording instruments in a model is sufficient for generating plausible native signals and underlying membrane mechanisms from signals that are distorted by the recording apparatus.

Instrumental and structural parameters jointly define signal distortion in recordings from small neuronal structures

In addition to providing a useful tool for predicting and correcting instrumental distortions our simulations confirmed that complete elimination of the instrumental disturbance was not possible during recordings (Ritzau-Jost et al., 2021), since substantial difference persists between the measured and native APs, even when the capacitance compensation reached the maximally attainable level (see **Figure 5C**). The model raised the possibility that inadequate local signal generation also significantly contribute to the alterations in AP shapes in addition to filtering that affects recordings through patch pipettes. We refer to this effect as observer effect based on the analogy with the concept introduced in the field of physics for situations where the measurement inevitably changes the measured parameter. The observer effect can be quantified as the difference between local APs (signals in the structure when pipette is present) and native APs (signals without the presence of any instrument, **Figure 4G and H**). We quantified the relative contribution of filtering and observer effects to the total

17

362   instrumental distortion in different experimental situations. Specifically, we varied pipette parameters,

363   compensation settings and the size of the recorded cell (size was set to as $C_{cell} = 1$ pF and 10 pF, corresponding

364   to the size of axons or small caliber dendrites and small cell bodies, respectively) in a reduced model which

365   included only a single neuronal compartment with the instrumentation and compared the half-widths of APs

366   (**Figure 7**). First, we isolated the filter effect by comparing simultaneous AP signals in the pipette and in the cell

367   (measured versus local AP).
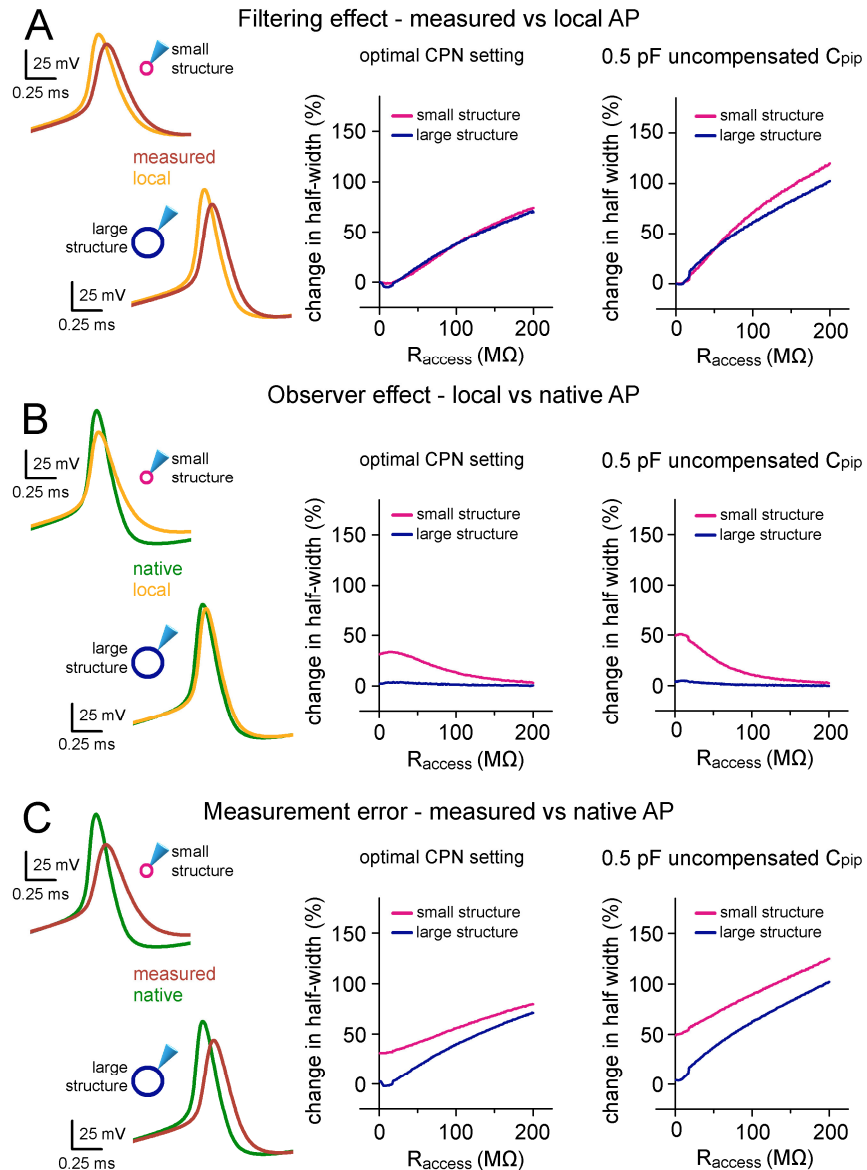
368

369   **Figure 7. Instrumental and structural parameters cooperatively determine signal distortions in recordings from**
370   **small neuronal structures**

18

(A) On the left, the differences between the waveforms of the same APs within the pipette (measured) and in the two hypothetical cells (local) highlight the filtering effect of 70 MΩ R_{access}. Only the size of the membrane surface were different in the two spherical structures, resulting in 1 and 10 pF biological capacitance, which correspond to small axonal and small somatic recordings. Graph in the middle summarizes the filtering effect quantified as the difference in AP half-width over a wide range of R_{access} in the small and large spherical cells. The right graph summarizes the filtering effect in simulations where suboptimal capacitance neutralization was applied (6.3 pF instead of 6.8 pF).

(B) Using the same simulation environment as in panel A, the observer effect was quantified as the difference between the local AP and the native AP waveform. Thus, this data represents the isolated influence of the instrument on local signal generation.

(C) To quantify the measurement error we demonstrate the difference between the measured AP and the native AP waveform in the same conditions as above. Thus, this is the sum of the filtering and observer effects.

In accordance with the general notion (Barbour, 2014), high R_{access} significantly filters fast voltage transients and allowed faithful measurement only in a confined R_{access} range (R_{access} that causes 10% AP signal widening: 47 MΩ for small cell and 41 MΩ in case of larger cell; **Figure 7A**, left). Furthermore, when uncompensated capacitance was added to the circuit by reducing the applied capacitance neutralization (-0.5 pF), the recording became more vulnerable and reliable recordings needed better R_{access} (R_{access} with 10% distortion: 20 MΩ for small cell and 17 MΩ in case of larger cell; **Figure 7A**, right).

Next, we isolated the observer effect by comparing the local and native AP shapes with or without the presence of the recording instrument (**Figure 7B**). The observer effect was always negligible in the case of the larger simulated biological structure as the capacitance added by the pipette was insignificant compared to the cellular parameters. In contrast, when the structure was smaller the structure had to discharge the remaining instrumental capacitance, which was in in this case in the range of C_{cell}, resulting in significant observer effect on the recorded AP shape (**Figure 7B**). Consistent with this hypothesis, observer effect was larger in simulations with additional uncompensated C_{pip} (mean change in AP half-width in the R_{access} range of 1-50 MΩ: 31.03±0.32 % vs. 40.54±1.14 %, optimal CPN vs. CPN with 0.5 pF uncompensated C_{pip}, respectively; **Figure 7B**). Intriguingly, the observer effect showed a reversed dependence on the R_{access}. It was the most pronounced when R_{access} was low. The larger

398   R_{access} presumably isolates the residual instrumental capacitance from the cell and consequently weakens the

399   instrumental impact.

400   Finally, by comparing the measured and native signals we assessed the overall measurement error. In case of the

401   larger simulated structure, the overall measurement error is dominated by the filtering effect (**Figure 7C**). In

402   contrast, when C_{cell} is small, the observer effect contributes significantly to the total error. Interestingly, the

403   complementary changes in the two effects make these recordings less sensitive to changes of R_{access} and the error

404   is similar when the R_{access} is low or high (**Figure 7C left**). The results confirm that residual uncompensated pipette

405   capacitance further deteriorate the difference between native and measured AP signals **(Figure 7C left).** Similar

406   conclusions can be drawn regarding other AP parameters as well (**Supplementary Figure 6**). Altogether, these

407   model simulations demonstrated that measurement errors in patch-clamp recordings depend not purely on the

408   pipette parameters but the size of the recorded structure itself has influence on the signal distortion.

409   Finally, to confirm the above findings on the error sources in a native biophysical structure we repeated the above

410   tests in a reconstructed MF that was labeled during somatic recording that ensured more intact axonal arborization

411   (**Figure 8A**). In this case the simulations ran with fixed instrumental parameters (6.74 pF C_{tot} and 60 MΩ R_{access},

412   with 6.8 pF capacitance neutralization and 60 MΩ bridge balance correction; **Figure 8A, B and C**). We evoked

413   APs along the axon and compared the pipette measured, local and native AP waveforms to determine the

414   contribution of the observer and filtering effects to the instrumental signal distortion and their dependence on the

415   local biophysical environment (**Figure 8A, B and C**). In agreement with the single compartment simulations

416   (**Figure 7**), observer effect had a major contribution to the overall measurement error (change in AP half-width:

417   7.02 ± 1.02 %, 34.03 ± 4.59 % and 43.26 ± 4.51 % for pipette filtering, for observer effect and for total

418   measurement error, respectively, n=941 locations; **Figure 8A, B and C**). As it is expected from the fixed

419   instrumental parameters, pipette filtering was similar in small and large diameter sections of the axon. In contrast,

420   the size of the observer effect was much larger in smaller axonal structures. Consequently, the measurement error

421   was also the largest in the smallest diameter sections (**Figure 8B**). Importantly, minima in observer effect coincide

422   with larger local capacitance, which originate from the large mossy fiber boutons in the CA3 area and branching

423   points in the hilus. Indeed, the overall measurement error showed similar inverse correlation to local capacitance

424   (R^2=0.68, power) as the observer effect (R^2=0.75, power) while the pipette filtering was structure-independent

425   (**Figure 8D-F**). These findings confirm that measurement error critically depends on the local biophysical

426   environment.
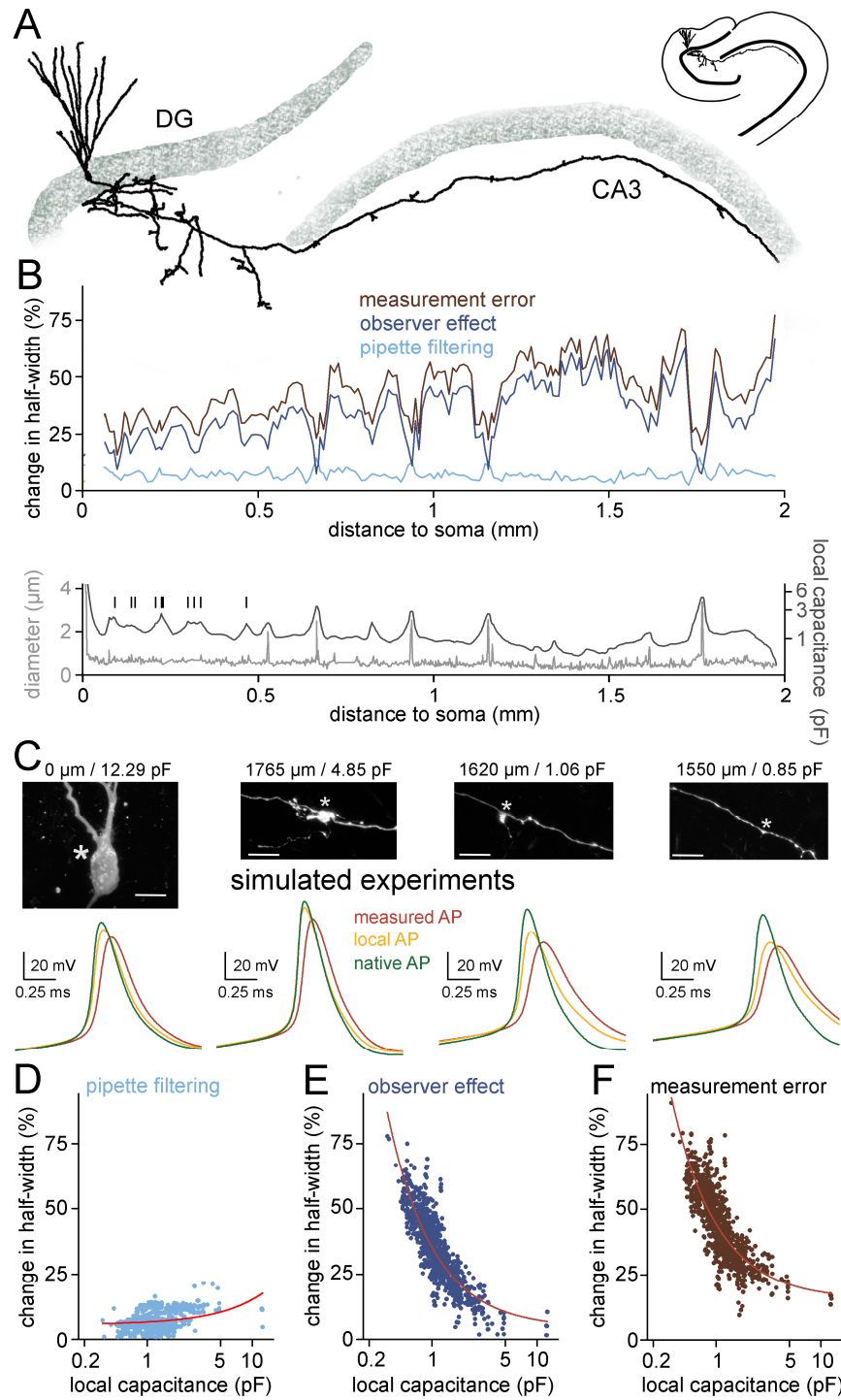
428   **Figure 8. Measurement error along the axon is inhomogeneous and depends on the local biophysical environment**

(A) Morphology of a somatically labeled complete granule cell that was used for simulating hypothetical recordings along its axon.

(B) Top, observer- and filtering effects (dark blue and light blue, respectively) together with the overall measurement error (brown) in simulated axonal measurements plotted against the somatic distance of the recording position. Each value represent average of 5 individual measurements in each 10 µm segments. Bottom, axonal diameter (grey) and local capacitance (black) as a function of somatic distance. Vertical bars indicate the branch points of hilar axon collaterals. Notice that signals that derive from axonal segments that are closer to the soma are less affected by the observer effect due to the capacitive "load" of the somatic membrane.

(C) Representative simulated recordings from the soma and different axonal sites and confocal images of the simulated recording site (same cell as in panel A). Corresponding somatic distances and local capacitances are indicated on the top. Asterisks mark the recording positions in the simulations. Scale bar=10 µm.

(D) The filtering effect showed only weak correlation with the local axonal capacitance (n = 941 simulated recordings, R^2 = 0.13, linear fit). Circles represent the filtering effect at independent measurement sites along the same axon. Note the logarithmic scale of the x-axis.

(E) The observer effect showed significant correlation with local axonal capacitance (n = 941 simulated recordings, R^2 = 0.75, fitted with power function).

(F) Correlation between the total measurement error and the local axonal capacitance (n = 941 simulated recordings, R^2 = 0.68, fitted with power function).

Discussion

Here we developed a measurement-based, highly realistic model representation of the recording instrument that faithfully replicates actual patch-clamp recordings when combined with the detailed morphological reconstruction of the recorded structure. Simulation of the complete experimental condition allows for eliminating the instrumental distortions that are inevitably contaminates signals from small neuronal processes, such as axons. This realistic model also enabled us to determine the extent and sources of perturbations that contaminate electrophysiological signals. The results showed that physical parameters of the measuring instrument and the local biophysical properties of the recorded structure and their quantifiable interactions define the errors in voltage

456   measurements. Consequently, signal deterioration potentially arise from the altered local signal generation instead

457   of pipette filtering in small axonal recordings.

458   The core hypothesis behind our study is that realistic *in silico* representation of recording instruments together

459   with the detailed morphology and biophysics of the recorded structure provide a better understanding of signal

460   distortions present in direct voltage recordings and offers an applicable offline approach to predict native signals

461   from distorted recordings. The combined simulation of the experimental conditions and the morphology was

462   proved previously to be an ideal tool to describe technical limitations associated with VC measurements and to

463   correct the recorded signals from those distortions (Beaulieu-Laroche & Harnett, 2018; Major et al., 1994;

464   Schaefer, Helmstaedter, Sakmann, & Korngreen, 2003; Silver, Traynelis, & Cull-Candy, 1992; Spruston, Jaffe,

465   Williams, & Johnston, 1993). However, these simulations have not included the complete recording instruments,

466   which are known to impose significant distortions on the recorded signals, especially when the biological source

467   is physically small, such as small axons. Other efforts corrected distortions of measured voltage signals by

468   estimating the transfer functions of the specific recording instrument (Brette et al., 2008; Jayant et al., 2017;

469   Magistretti, Mantegazza, de Curtis, & Wanke, 1998). Although such formulations are computationally efficient,

470   they could not be applied to the variable individual contribution of circuit components (e.g. pipettes, C_{pip} and

471   R_{access} compensatory elements), which imposes different signal distortions, such as filtering or instrumental

472   capacitive load. Here, we implemented the pipette and all amplifier elements as individual circuits as they were

473   actually built in the complete system and showed that the idealized instrument is sufficient to replicate the

474   behavior of the complete measuring instrument and its compensatory capabilities (**Figures 1, 2 and 3**). Thus, we

475   assume that implementing these components will allow adapting the model to other amplifier types. One of the

476   unexpected findings of our study is the uneven capacitance distribution of recording pipettes (Benndorf, 1995).

477   Majority of the total C_{pip} originate from the first two and a half mm from the tip (**Figure 3**). The gradual increase

478   of relative wall thickness from the tip explains the larger contribution of the tip. Although the relative wall

479   thickness was found to be constant previously for borosilicate glass capillaries (Benndorf, 1995) we observed

480   decreased relative wall thickness toward the tip that explains the larger capacitive contribution of the tip.

481   To outline a feasible application, we utilized the complete instrumental model to correct the shape of APs directly

482   recorded from a small axon terminal of a hippocampal mossy fiber. The size of this bouton (largest diameter: 0.7

483   µm) was in the range of typical cortical axon terminals and was much smaller than the famous large mossy fiber

484   terminals. The complete instrumental model in combination with the realistic axonal morphology and biophysics

485   faithfully replicated the measured voltage signals (**Figures 4, 5 and 6**), including the signal artefacts and distorted

486   fast APs. The simulation resulted in ionic currents and conductances that matched with previous results obtained

487   with direct MF recordings from large boutons (**Figure 4E and F**) (H. Alle et al., 2011; Henrik Alle et al., 2009;

488   Geiger & Jonas, 2000). Consequently, the retrieved native axonal APs were brief events with large amplitude

489   (**Figures 4, 5 and 6**) whose shape closely resembled to the spike waveforms reported for the large axon terminals

490   of the same axon (Henrik Alle et al., 2009; Geiger & Jonas, 2000). The simple Hodgkin-Huxley type conductance

491   models with six free parameters were sufficient to restore the experimentally recorded MF AP waveforms.

492   Although APs in the distal MFs can be described with a similar standard Hodgkin-Huxley type gating (Engel &

493   Jonas, 2005; Ohura & Kamiya, 2018), AP simulation in other neuron types or in other subcellular elements

494   required more detailed kinetic schemes (Stefan Hallermann et al., 2012; Ritzau-Jost et al., 2014; Ritzau-Jost et

495   al., 2021; Schmidt-Hieber & Bischofberger, 2010). Therefore, implementation of more elaborated conductance

496   models and inclusion of additional conductances can further improve our simulations and adapt to multiple

497   activity regimes, such as the plasticity of AP shapes during sustained activity (Geiger & Jonas, 2000).

498   The complex model allowed us to dissect the sources of errors that contaminate recordings from small biological

499   structures. As previously described for small, electrotonically compact neurons (D'Angelo, De Filippi, Rossi, &

500   Taglietti, 1995; Goodman, Hall, Avery, & Lockery, 1998; Rohrbough & Broadie, 2002), we found that even with

501   careful capacitance neutralization, the capacitive load added by the recording instrument substantially altered the

502   intrinsic electrical behavior of the axon (**Figures 4 and 5**). Using a simplified neuronal representation, we

503   confirmed with that instrumental capacitance effectively attenuates the action potentials in small neuronal

504   structures (**Figure 7**) emphasizing again that C_{pip} reduction can substantially improve the accuracy of the

505   measured voltage signal (Dudel, Hallermann, & Heckmann, 2000; Levis & Rae, 1993; Ogden & Stanfield, 1994;

506 Ritzau-Jost et al., 2021; Sakmann & Neher, 1983). Interestingly, we have shown that increase in the R_{access} reduced

507 the instrumental impact on the cellular electrogenesis (probably due to effective electrical isolation of the neuronal

508 structure from the recording pipette) suggesting that high impedance recording can have also advantages when

509 experimental subject is small. The high impedance recordings may reduce the complexity of *post hoc* AP

510 reconstitution as in this case the predicted AP shape depends only on the pipette filtering (Jayant et al., 2017).

511 One of the major findings of our study is that instrumental and cellular factors define the accuracy of CC

512 experiments not in isolation from each other, but their interaction is equally important. This was the most apparent

513 when we examined the cellular contribution of the overall measurement error along a reconstructed MF which

514 forms varicosities with different diameter. Thus, the differently sized axon segments provides different local

515 biophysical conditions (**Figure 8**). In this arrangement, which is characteristic to all axons at a various degree

516 (i.e. the size of the terminals and axonal shaft varies), the observed inverse relationship between local capacitance

517 and the measurement error highlight the importance of structural details on direct axonal recordings.

518 A more general consideration is that the target-size-dependent effects are not specific to the axonal recordings.

519 Experiments that target small cellular structures, whose electrical parameters are comparable to the capacitance

520 introduced by the measuring instrument, are potentially subject to the distortions quantified in our study. The

521 target-dependent measurement errors are not specific to the action potential firing either. In fact, the typically

522 high conductance densities in axons (Hu & Jonas, 2014; Ritzau-Jost et al., 2014) can partly compensate for the

523 observer effect. Depending on the local biophysical environment, the recording instruments can induce substantial

524 observer error in dendritic membrane potential as well.

525

Methods

527 Experimental procedures were made in accordance with the ethical guidelines of the Institute of Experimental

528 Medicine Protection of Research Subjects Committee (MÁB-7/2016, PE/EA/48-2/2020).

529

25

530   *Constraining the amplifier model*

531   *The model cell.* Electrical components of the customized model cell (test#3 circuit, modified type 1U, Molecular

532   Devices) were connected through conductive metal slots taken from a circuit breadboard allowing the change of

533   circuit components without the need for soldering that would introduce variable stray capacitance (Supplementary

534   Figure 1). We used non-inductive, low-noise resistors: resistors either originally present in the 1U model cell,

535   10MΩ and 500 MΩ, or Ohmite SLIM-MOX10203 series, 20-100MΩ. Stray capacitance of each elements of the

536   test circuits (including the resistors and their slots) was characterized in VC mode by measuring the capacitive

537   load associated with the introduction of the given circuit element. All capacitors were considered ideal, that is,

538   without any resistive component.

539   *Boosting unit.* We implemented a simplified boosting unit (Sigworth, 1995) in which capacitors were fixed (100

540   pF and 120 pF) while resistors were directly fitted to reproduce the capacitive current response in the test#1

541   configuration. Late phase of the response profile (starting 24 μs after the stimulus onset) has particular importance

542   because artefacts in that temporal domain can contaminate measured biological signals, therefore, this part of the

543   signal was heavily weighted (850x) during the adjustment of the boosting unit.

544   *VC capacitance compensation:* Both CPf and CPs circuits were designed as described previously (Sigworth,

545   1995).

546   *Stray capacitance of the CC circuit.* To optimize the circuitry of CC model, we performed measurements with

547   test#3 circuit, where pipette parameters (10MΩ, 2.8 pF) and the size of the cell-equivalent resistor (500 MΩ) were

548   fixed, only cellular capacitance varied from 0.75 pF to 46.7 pF. We applied short current stimuli (-50 to -200 pA,

549   3 ms) to elicit voltage responses with the maximal attainable capacitance neutralization or without CPN. Traces

550   recorded in the absence of CPN allowed us to characterize the total capacitive load of the CC circuitry. The model

551   most accurately reproduced the real voltage responses when a 0.76 pF stray capacitance was added at the amplifier

552   input node (C_{CC} on Figure 1).

553   *Capacitance neutralization (CPN)*. We implemented CPN in two steps. First, we added an idealized positive

554   feedback loop, where the compensation through the C_{inj} can be modulated with the gain of an operational

555   amplifier. This simple circuit representation was sufficient to reproduce the neutralizing capability of the real

556   amplifier, that is, equal CPN settings resulted in the same level of compensation in the model as in the real

557   experiments. Next, we reproduced the characteristic CPN-related stimulus artefacts that are present in typical

558   current clamp measurements. We placed a resistor (R_{CPN}) and an inductor (L_{CPN}) to the CPN path (Figure 1) and

559   tuned their parameters by direct fitting of the model voltage responses to the experimental data (examples are

560   shown on Figure 2D).

561   *Bridge balance compensation (BB)*. To recreate the BB circuit, we created a reference signal from the command

562   equivalent to the voltage drop caused by 1 MΩ load resistance (Figure 1). Scaled version of that reference signal

563   was then subtracted from the pipette voltage for the correction.

564   *Bessel filters*. We added filters to the amplifier model to match of our actual biological recordings. We added an

565   active linear filter consisting of two cascaded Sallen-Key filter stages (Figure 1). Filter parameters were set

566   according to an available filter design tool (https://www.analog.com/designtools/en/filterwizard/) to produce

567   output with four pole low-pass Bessel filter characteristics. All recordings were made with bypassed filtering

568   mode and we applied 100 kHz lowpass filter throughout the simulations.

569   *Pipette parameter measurements*

570   We used typical borosilicate glass capillaries (BF150-75-10, Sutter Instruments, Novato, CA) to fabricate pipettes

571   that are suitable for recordings from small axons. To implement these high impedance pipettes into the model we

572   measured their actual parameters. First, we assessed the actual pipette capacitance as a function of the tip distance

573   by dipping known part of the recording pipettes into the recording solution. Pipette position was measured by the

574   x axis values of the motorized micromanipulator (SM5 controller with Mini unit, Luigs und Neumann, Ratingen,

575   Germany). First, we recorded the total capacitance of the instrumentation in open circuit VC mode when the

576   pipette was out of the solution. Then, we gently moved the pipette to a position where the tip intermittently

27

577 reached the surface of the fluid characterized by the appearance of short conductive periods in the recorded VC

578 signal. Then, the pipette was pushed forward to the solution to reach a position where the conductive state became

579 stable (typically <5 μm forward movement). Starting from this tip position point, we systematically increased the

580 length of the dipped part and quantified the capacitance in VC by integrating the first 50 μs of the transient

581 response to a -20 mV voltage step. Integrated area was divided by the voltage step amplitude to convert the electric

582 charge to capacitance.

583 To measure distribution of resistance along the pipettes, we broke off a known length of the pipette and measured

584 the resistance of the remaining part in VC mode. First, we moved the pipette tip to a defined position under the

585 objective and recorded its resistance. After withdrawal of the pipette, we broke the tip by gently touching it with

586 a piece of lens cleaning tissue. The newly formed pipette tip was then positioned back to the reference position

587 on the image. We determined the length of the broken pipette parts by reading the difference of the positioning

588 motor. Resistance was measured in VC mode using -2 to -20 mV steps. We repeated the breaking process for

589 each pipettes several times (1x-8x, using 22 pipettes in total).

590 We visualized the outer/inner diameter ratio (R_{OI}) of the recording pipettes using a grinding system that gradually

591 cut them in half. This measurement allowed to avoid the optical distortions caused by the lens effect of the

592 cylindrical glass. The recording pipettes (the first 8-12 mm from the tip) were embedded into epoxy resin on a

593 microscope slide. Pipettes were longitudinally grinded with a coarse-grained aluminium-oxide abrasive disc (grit

594 size=600) until we reached the surface of the pipettes. Then, the grinding was occasionally interrupted to check

595 the surface and cross-section of the pipette under a transmitted light microscope (Leica DM2500 microscope, 5X-

596 100X magnifications). As the plane of the pipette tip was approached, we switched to fine-grained abrasive discs

597 (grit size=6000). The images obtained from different cross section levels were then used to measure the pipette

598 diameters (Adobe Photoshop 5.0). The diameter data were included only from those focal planes for distinct

599 segments of the pipette tips, where the outer diameter was the largest and the relative wall thickness was the

600 smallest. We assumed infinite pipette wall resistivity in the model.

28

601 *Slice preparation and electrophysiology*

602 Hippocampal slice was prepared from a 29 days old Wistar rat as previously described (Brunner & Szabadics,

603 2016). In brief, the animal was deeply anaesthetized with isoflurane. After decapitation, the 350 μm thick slice

604 was cut with Leica VT1200S vibratome in ice-cold cutting solution (85 mM NaCl, 75 mM sucrose, 2.5 mM KCl,

605 25 mM glucose, 1.25 mM NaH_2PO_4, 4 mM $MgCl_2$, 0.5 mM $CaCl_2$, and 24 mM $NaHCO_3$) in an orientation

606 optimized to preserve the mossy fibre tract in the hippocampal CA3 area (Bischofberger, Engel, Li, Geiger, &

607 Jonas, 2006). The slice was incubated at 32 °C for 60 minutes after sectioning, and was stored at room temperature

608 until the experiment. The recording solution was composed of 126 mM NaCl, 2.5 mM KCl, 26 mM $NaHCO_3$, 2

609 mM $CaCl_2$, 2 mM $MgCl_2$, 1.25 mM NaH_2PO_4, and 10 mM glucose (equilibrated with 95% O_2 and 5% CO_2 gas

610 mixture). The pipette was filled with an intracellular solution containing 90 mM K-gluconate, 43.5 mM KCl, 1.8

611 mM NaCl, 1.7 mM $MgCl_2$, 0.05 mM EGTA, 10 mM HEPES, 2 mM Mg-ATP, 0.4 mM Na_2-GTP, 10 mM

612 phosphocreatine, 8 mM biocytin and 20 μM Alexa Fluor 594 hydrazide (pH=7.25). The recordings were

613 performed at 35 °C. For patching, axon was visualized with an upright IR-DIC microscope (Eclipse FN-1; Nikon)

614 equipped with high-numeric aperture objective (Nikon 1.1 NA, Apo LWD 25 W), oil condenser (Nikon D-CUO

615 DIC Oil Condenser, 1.4 NA) and a sCMOS camera (Andor Zyla 5.5). After the recordings the Alexa Fluor 594-

616 labelled structure was visualized in situ using a confocal system (Nikon Eclipse C1 Plus). Then, the slice was

617 fixed for further morphological experiments (see below).

618 To record from the individual small MF terminal, we searched for visually identifiable axonal structures under

619 the guidance of the DIC optics in the *stratum lucidum* of the CA3 area, whose size was smaller than those of the

620 typical large mossy fiber boutons. The patch pipette was pulled from borosilicate glass capillary (inner diameter:

621 0.75 mm, outer diameter: 1.5 mm, Sutter Inc.). After the seal formation, we manually carefully compensated the

622 C_{pip} in VC mode. Compensated capacitive responses to -20 mV step command were then recorded and the average

623 of 164 sweeps served as target for tuning the C_{pip} in the model. After establishing the whole-cell configuration by

624 applying sudden negative pressure, we switched to CC mode to record the passive and active membrane responses

625 from the axon with different CPN compensation. All recordings were collected with a MultiClamp 700B amplifier

626 (Molecular Devices) without filtering (filter bypassed) and digitized with Digidata1440 A/D board (Molecular

627 Devices) at 250 kHz sampling rate using the pClamp10 software package (Molecular Devices). At the end of the

628 experiment, we collected preliminary morphological data by imaging the Alexa Fluor 594 signal with the confocal

629 system. The obtained z stack image was then used to confirm the MF identity (evidenced by the presence of a

630 large MF terminal along the recorded axon, Figure 4B) and for the documentation of the recording position.

631 *3D morphological reconstruction*

632 After the recording, slice was fixed overnight at 4°C in 0.1 mM phosphate buffer containing 2% PFA and 0.1%

633 picric acid. The slice was then re-sectioned (to 60 μm) and the sections were incubated overnight with Alexa

634 Fluor 594-conjugated streptavidin in 0.5% Triton X-100 and 2% normal horse serum to reveal the biocytin signal.

635 To investigate the detailed morphology,the recorded axon was imaged with a confocal system (60X objective,

636 Plan Apo VC, NA=1.45, Nikon C2, x-y pixel size:0.08-0.1 μm, z-step: 0.1-0.15 μm). High resolution

637 reconstructions were done automatically by the Vaa3D software (Peng, Bria, Zhou, Iannello, & Long, 2014; Peng,

638 Ruan, Long, Simpson, & Myers, 2010; Peng, Tang, et al., 2014).

639 *Implementation of the seal in the model*

640 The seal was represented as a single resistor (R_{seal}) connected in parallel to the cell. To estimate the R_{seal} in the

641 axonal recording, first we calculated the ratio (R_{ratio}) between the cellular input resistance (R_{cell}) and the R_{seal}

642 based on the voltage shift produced by the shunt conductance of seal (Perkins, 2006):

$$V_{measured}/V_{rest} = R_{ratio}/(1 + R_{ratio})$$

644 where $V_{measured}$ is the recorded voltage, V_{rest} is the native resting membrane potential. R_{seal} and R_{cell} were then

645 calculated from the measured input resistance ($R_{in,measured}$) and from the R_{ratio} using the equations:

$$1/R_{cell} = 1/R_{in,measured} - 1/R_{seal}$$

647 where:

$$R_{seal} = ratio * R_{cell}$$

30

649   The apparent resting membrane potential of the recorded MF axon was -75.2 mV, close to the resting membrane

650   potential previously reported for the somata and axons of granule cells (~ -80 mV (Brunner & Szabadics, 2016;

651   Martinello, Giacalone, Migliore, Brown, & Shah, 2019; Ruiz, Campanac, Scott, Rusakov, & Kullmann, 2010;

652   Schmidt-Hieber, Jonas, & Bischofberger, 2004; Staley, Otis, & Mody, 1992)). This moderate shift, caused by the

653   leak through the seal, suggests orders of magnitude larger R_{seal} compared to the axonal input resistance. Indeed,

654   we calculated 65.64 GΩ R_{seal} and 3.94 GΩ R_{cell} for the recording assuming -80 mV resting membrane potential.

655   Accordingly, we applied 65.64 GΩ R_{seal} in the AP reconstitution model (Figures 4, 5 and 6), while R_{seal} was set

656   to 50 GΩ in all other simulations. To compensate for the seal-induced depolarizing voltage shift, baseline

657   membrane potential in the model was adjusted by constant current injection to match those of the experimental

658   data.

659   *General simulation parameters*

660   Cellular membrane parameters were assumed to be spatially uniform, unless stated otherwise. Potassium and

661   sodium equilibrium potentials were set to -77 mV and +70 mV, respectively and we assumed -80 mV reversal

662   potential for the leak conductance in active models. Simulations ran with 4 µs and 0.5 µs temporal resolution, in

663   CC mode and in VC mode, respectively.

664   *Fitting procedures*

665   We fitted the model responses to the experimental data to minimize the sum of squared error between them using

666   the Brent's PRAXIS optimization algorithm embedded in NEURON. For C_{pip} estimation, a 5 ms long trace was

667   considered with 2.5 ms baseline before the stimulus. For passive parameter estimations, we weighted the voltage

668   response evoked by short current stimulus (25.8 ms from the stimulus onset, 3X) in order to equalize the

669   contribution of short- and long pulse responses to the total error. For AP reconstruction, fitting interval started

670   with 2.6 ms long baseline period before the stimulus onset. The actual APs were weighted eight-fold, starting 0.5

671   ms before the peak. The optimization ended 1.5 ms following the AP peak to avoid the contamination of the

31

672 parameter estimation with afterdepolarization related mechanisms not implicated in the model (Martinello et al.,

673 2019; Ohura & Kamiya, 2018).

674 We used sodium and potassium conductance mechanisms with canonical Hodgkin-Huxley gating scheme, in

675 which not only the density can be freely adjusted but also the kinetics and the voltage dependence of the two

676 types of conductance. For this, we modified the built-in Hodgkin-Huxley mechanisms of NEURON by

677 introducing rate-scaling factors (scNa and scK) to adjust the speed of model channel operation. The originally

678 implemented temperature scaling was removed from the mechanisms. In addition, we used global voltage shifts

679 (vsNa and vsK) to modulate the voltage dependence of the channels. Altogether, free parameters ($g_{max}Na$, $g_{max}K$,

680 scNa, scK, vsNa, vsK) were constrained to obtain an ideal model of the AP waveform measured in our various

681 experimental settings. Because the R_{access} can change during the recordings, this parameter was set individually

682 for each target trace. Optimization of the individual AP fits was initiated from four parameter sets that allows

683 exploration substantial part of the parameter space (Supplementary Figure 3A). The parallelized codes for AP

684 reconstitution were run on the Comet supercomputer through the Neuroscience Gateway portal (Sivagnanam et

685 al., 2013). To assess the quality of individual fits, their mean squared error was normalized to the baseline variance

686 of the actual target trace. Of the results of the four parallel optimizations, the solution where the normalized error

687 was the smallest was accepted as the best fit. Fit was rejected when the normalized error was larger than 10.

688 Fitting of 2 of the original 90 target APs did not resulted in solutions, which met this criterion. These APs were

689 excluded from the analysis (both were obtained with 7.386 pF CPN).

690

691 *Assessments of the reliability of optimizations*

692 *In silico* reconstruction of the complete experiment consisted of subsequent optimization steps (Supplementray

693 Figure 2A). First, we used VC data to set actual pipette parameters (1). After adding the model instrumentation

694 and the detailed morphology of the recorded structure to the model, we tuned the passive cellular parameters

695 together with the R_{access} (2). Next, we equipped the model structure with active sodium and potassium

32

696 conductances and adjusted their properties to match model responses the experimentally recorded AP waveform

697 (3). Finally, having established the appropriate conductance sets, we obtained the native behavior of the axon (4).

698 The reliability of the fitting procedures were tested with artificial traces with Gaussian noise.

699 To assess the accuracy of C_{tot} estimation, we generated target traces by simulating on-cell VC experiments. The

700 model always recovered correct C_{tot} value (proportion of fitting estimations within 10% error to the correct value:

701 100 %, n=990 optimizations, Supplementary Figure 2A and B) irrespective to the C_{tot} (5.8-13.7 pF) and noise

702 level (SD=0-35.3 pA) of the targets, which confirms the high sensitivity of VC based C_{pip} estimation.

703 To test the reliability of cellular passive parameter and R_{access} prediction, we created a hypothetical axon with

704 biologically plausible diameter distribution (log-normal distribution with mean of 0.6 µm and variance of 0.4

705 µm^2). We attached the model axon to the pipette and generated hypothetical CC measurements with long and

706 short current stimuli (C_m range: 0.5 - 1.5 uF/cm^2, R_m range: 10 - 100 kΩ/cm^2, R_i range: 50 - 250 Ω*cm, R_{access}: 50

707 - 400 MΩ, noise SD = 1.73 mV). We fitted these synthetic targets from a single initiation parameter set (C_m: 1

708 pF/cm^2, R_m: 50 kΩ/cm^2, R_i: 150 Ω*cm, R_{access}: 150 MΩ). 75 % of optimizations resulted in acceptable results,

709 that is, the fit error was less than 10-times the baseline variance of its target. In those successfully fitted cases the

710 predicted parameters were close to their predefined values (proportion of fitting estimations within 10% error to

711 the correct value: C_m: 90.83 %, R_m: 97.66 %, R_i: 81.88 %, R_{access}: 82.3 % n= 469 optimizations, Supplementary

712 Figure 2C).

713 We also verified the reliability of the prediction of native AP shapes in independent simulations (Supplementary

714 Figure 2D and E). For this we generated diverse AP waveforms using independent, sophisticated sodium and

715 potassium conductance mechanisms (using 8-state kinetic schemes obtained from (Stefan Hallermann et al., 2012;

716 Schmidt-Hieber & Bischofberger, 2010) in a single compartment neuron (R_{access}=100 MΩ, C_{pip}=6.74 pF, BB

717 compensation=100 MΩ, CPN compensation= 6.85 pF, R_{seal}=50 GΩ, noise SD: 0.45 mV). Our standard fitting

718 routine reliably retrieved the shapes of APs.

719 *Systematic errors in model predictions*

33

720 We also examined the potential impact of systematic error sources on model predictions. Such potential error can

721 originate from inaccuracies of the morphological reconstruction. Post hoc anatomical processing can result in

722 considerable tissue shrinkage. Additionally, diameter of thin axonal processes is close to the resolution limit of

723 light microscopy. To evaluate the potential effects of inaccurate anatomical representation of the recorded axon,

724 we artificially altered the reconstructed morphologies and tested how the recovered native APs were affected.

725 The axonal diameters were either homogeneously increased by 160 nm or reduced by 180 nm (axons were not

726 allowed to shrink below 100 nm). As expected, recovered passive parameters and active conductance densities

727 scaled with the diameter to compensate for the altered morphological dimensions (Table 1). However, as the

728 model re-adjusted the local electrical environment by scaling the membrane properties, the predicted intra-axonal

729 and native AP waveforms remained remarkably similar in spite of the large changes in the morphology and

730 passive membrane parameter.

731 R_{seal} provides an additional error source because its calculation depends on the native resting membrane potential,

732 which can not be assessed directly (i.e. measurements start in cell attached mode). Therefore, we defined the

733 theoretical lower limit for the R_{seal} in the direct axonal recording; when native resting membrane potential equals

734 with the potassium equilibrium potential (-93 mV with the solutions used in the experiment) R_{seal} would be only

735 20.58 GΩ. Re-optimization of the model using this small R_{seal} caused only minor alterations in the predicted

736 conductances and AP parameters (reduced R_{seal} model, Table 1). Altogether, these control simulations suggest

737 that potential systematic errors have marginal impact on the primary results of the manuscript.

34

738

		standard model	reduced R_{seal}	thick morphology	thin morphology
Passive parameters	$R_m(k\Omega/cm^2)$	60.01	72.92	62.97	38.88
	$C_m(\mu F/cm^2)$	0.65	0.62	0.62	0.99
	$R_i(\Omega*cm)$	147.3	141.54	208.08	56.78
	normalized error	2.96	3.05	2.95	3.18
active conductances for APs recorded with CPN=6.5 pF	$gNa(mS/cm^2)$	159.02±1.73	160.24±2.1	150.24±1.86	229.79±3.57
	$gK(mS/cm^2)$	5.83±0.46	5.46±0.04	5.33±0.04	12.74±0.56
	normalized error	5.2±0.16	5.09±0.16	5.22±0.16	5.72±0.19
active conductances for APs recorded with CPN=7 pF	$gNa(mS/cm^2)$	151.7±0.95	150.29±1.06	142.27±0.97	232.6±1.5
	$gK(mS/cm^2)$	5.41±0.03	5.08±0.03	5.08±0.03	9.23±0.08
	normalized error	5.89±0.17	5.92±0.17	6.36±0.18	6.04±0.19
active conductances for APs recorded with CPN=7.386 pF	$gNa(mS/cm^2)$	160.03±1.47	142.26±1.17	144.38±1.23	249.13±2.44
	$gK(mS/cm^2)$	6.32±0.09	6.08±0.44	5.87±0.07	11.24±0.146
	normalized error	6.8±0.28	8.22±0.34	8.1±0.3	7.35±0.3
AP parameters (reconstructed measurement)	$dV/dt_{max}(mV/ms)$	363.26±0.93	369.87±6.04	354.99±0.8	372.7±0.96
	peak(mV)	9.01±0.12	9.01±0.49	8.98±0.12	9.24±0.12
	threshold(mV)	-45.28±0.07	-45.29±0.06	-45.17±0.07	-45.69±0.06
	half-width(ms)	0.52±0.002	0.52±0.004	0.51±0.002	0.52±0.002
AP parameters (local in the axon)	$dV/dt_{max}(mV/ms)$	453.11±2.54	453.82±2.53	450.44±2.34	481.59±3.06
	peak(mV)	21.96±0.12	21.23±0.12	22.13±0.12	22.34±0.11
	threshold(mV)	-35.88±0.09	-35.92±0.09	-36.01±0.09	-36.97±0.09
	half-width(ms)	0.48±0.002	0.49±0.002	0.48±0.002	0.49±0.002
AP parameters (native, I-step evoked)	$dV/dt_{max}(mV/ms)$	1064.81±5.1	1111.03±5.76	865.03±4.65	914.95±6.32
	peak(mV)	46.85±0.09	47.34±0.09	40.06±0.12	40.26±0.15
	threshold(mV)	-37.36±0.09	-37.64±0.09	-35.93±0.09	-36.7±0.09
	half-width(ms)	0.33±0.002	0.33±0.002	0.33±0.002	0.34±0.002
AP parameters (native, propagating)	$dV/dt_{max}(mV/ms)$	1605.96±9.75	1671.34±10.82	1609.7±10.18	1549.38±12.2
	peak(mV)	64.21±0.07	64.71±0.07	64.16±0.08	63.29±0.11
	AP width @-10 mV (ms)	0.36±0.002	0.35±0.002	0.36±0.002	0.36±0.002
	propagation velocity(ms)	0.45±0.001	0.48±0.002	0.46±0.002	0.43±0.002

n=30 AP reconstitution

739   **Table 1. Summary of parameters obtained from different model configurations**

740

741   *Simulations to explore the correlations between signal distortions and recording conditions (Figure 7)*

742   We used a single compartment with fixed 10 μm^2 surface area to represent neuronal structure in these simulations.

743   Electrical behavior of small and larger cells was set by scaling the active and passive biophysical parameters of

744   the compartment (for small cell: C_m=10 $\mu F/cm^2$, R_m=2 $k\Omega/cm^2$, g_{Na} density=1.5 S/cm^2, g_K density=0.4 S/cm^2; for

35

745   larger cell: C_m=100 µF/cm^2, R_m=0.2 kΩ/cm^2, g_{Na} density=15 S/cm^2, g_K density=4 S/cm^2). To keep R_{seal}/R_{cell} ratio

746   constant between the two conditions, R_{seal} was set to 50 GΩ and 5 GΩ, for small and larger cell, respectively.

747   The pipette capacitance was fixed to 6.74 pF while R_{access} was systematically varied in the range of 1-200 MΩ.

748   To mimic optimal recording configuration, the applied CPN settings (6.8 pF) closely matched with C_{pip}. APs were

749   elicited with 3 ms long current stimuli (30 pA and 160 pA for small and larger cell, respectively).

750   *Simulations to explore the correlations between signal distortions and axonal morphology (Figure 8)*

751   The detailed morphology of a somatically labeled granule cell was imported to the NEURON. Dendritic spines

752   were implemented by scaling two-fold the C_m and the leak conductance in dendrites. Passive parameters (R_i:150

753   Ω*cm, C_m:1 µF/cm^2, R_m:50 kΩ/cm^2) were constant otherwise. Active conductances (g_{Na} density=300 mS/cm^2,

754   g_K density=15 mS/cm^2) were homogenously distributed along the cell, except the initial part of the axon where

755   we applied higher channel densities (g_{Na} density=1200 mS/cm^2, g_K density=75 mS/cm^2) with left-shifted

756   activation and inactivation (10 mV in the hyperpolarized direction). To explore the distortions in axonal AP

757   recordings, position of recording electrode (C_{tot}=6.74 pF, R_{access}=60 MΩ, R_{seal}=50 GΩ, applied CPN=6.8 pF) was

758   systematically changed along the main axon (n=942 recording positions). APs were evoked by 3 ms long current

759   stimuli at each recording position. Amplitude of the injected current was automatically adjusted to evoke APs

760   ~1.5 ms (1.33 ± 0.01 ms delay, n=942 APs) after stimulus onset. Local capacitance was determined for each

761   recording position using idealized VC simulations in the absence of experimental instrumentation (built-in

762   SEClamp mechanism with 10 MΩ series resistance). For quantification, we integrated the first 100 µs of the

763   transient capacitive response to -20 mV voltage step. The resulted charge was divided by the voltage step

764   amplitude.

765   *Data analysis and statistics*

766   AP threshold was determined as membrane voltage where depolarization rate exceeded 20 mV/ms. AP amplitude

767   was calculated as the voltage difference between the absolute peak potential and the threshold. AP half-width was

768   defined as the spike duration at half of its amplitude. AP conduction velocity was determined by measuring the

769   temporal difference between AP peaks at the initiation and at the recording site.

770   Data were analyzed using pClamp (Molecular Devices), OriginPro (OriginLab) and Excel (Microsoft) Photoshop

771   (Adobe) and custom written NEURON or Python scripts. The relevant NEURON codes are available on GitHub

772   (https://github.com/brunnerjanos/amplifier-model). Voltage values are presented without correction for the liquid

773   junction potential. Normality of the data was assessed with Shapiro-Wilks test. Population data are presented as

774   mean ± s.e.m.

775

Acknowledgements

784

References

786   Acsady, L., Kamondi, A., Sık, A., Freund, T., & Buzsáki, G. (1998). GABAergic cells are the major postsynaptic targets of
787   mossy fibers in the rat hippocampus. *Journal of Neuroscience, 18*(9), 3386-3403.

788   Alle, H., Kubota, H., & Geiger, J. R. (2011). Sparse but highly efficient Kv3 outpace BKCa channels in action potential
789   repolarization at hippocampal mossy fiber boutons. *J Neurosci, 31*(22), 8001-8012. doi:10.1523/jneurosci.0972-
790   11.2011

791   Alle, H., Roth, A., & Geiger, J. R. (2009). Energy-efficient action potentials in hippocampal mossy fibers. *Science, 325*(5946),
792   1405-1408.

793   Araki, T., & Otani, T. (1955). Response of single motoneurons to direct stimulation in toad's spinal cord. *J Neurophysiol,
794   18*(5), 472-485. doi:10.1152/jn.1955.18.5.472

795 Barbour,   B.   (2014).   Electronics   for   electrophysiologists.   .   Retrieved   from
796   https://www.biologie.ens.fr/~barbour/electronics_for_electrophysiologists.pdf

797 Bean, B. P. (2007). The action potential in mammalian central neurons. *Nature Reviews Neuroscience, 8*, 451.
798   doi:10.1038/nrn2148

799 Beaulieu-Laroche, L., & Harnett, M. T. (2018). Dendritic Spines Prevent Synaptic Voltage Clamp. *Neuron, 97*(1), 75-82.e73.
800   doi:10.1016/j.neuron.2017.11.016

801 Benndorf, K. (1995). Low-noise recording. In *Single-Channel Recording* (pp. 129-145): Springer.

802 Bischofberger, J., Engel, D., Li, L., Geiger, J. R., & Jonas, P. (2006). Patch-clamp recording from mossy fiber terminals in
803   hippocampal slices. *Nature protocols, 1*(4), 2075.

804 Borst, J. G., & Sakmann, B. (1999). Effect of changes in action potential shape on calcium currents and transmitter release
805   in a calyx-type synapse of the rat auditory brainstem. *Philos Trans R Soc Lond B Biol Sci, 354*(1381), 347-355.
806   doi:10.1098/rstb.1999.0386

807 Branco, T., & Häusser, M. (2011). Synaptic Integration Gradients in Single Cortical Pyramidal Cell Dendrites. *Neuron, 69*(5),
808   885-892. doi:10.1016/j.neuron.2011.02.006

809 Brette, R., Piwkowska, Z., Monier, C., Rudolph-Lilith, M., Fournier, J., Levy, M., . . . Destexhe, A. (2008). High-resolution
810   intracellular recordings using a real-time computational model of the electrode. *Neuron, 59*(3), 379-391.

811 Brunner, J., & Szabadics, J. (2016). Analogue modulation of back-propagating action potentials enables dendritic hybrid
812   signalling. *Nature Communications, 7*, 13033.

813 Chao, O. Y., & Yang, Y.-M. (2019). Timing constraints of action potential evoked Ca2+ current and transmitter release at a
814   central nerve terminal. *Scientific Reports, 9*(1), 4448. doi:10.1038/s41598-019-41120-5

815 Cornwall, M. C., & Thomas, M. V. (1981). Glass microelectrode tip capacitance: its measurement and a method for its
816   reduction. *J Neurosci Methods, 3*(3), 225-232. doi:10.1016/0165-0270(81)90057-1

817 D'Angelo, E., De Filippi, G., Rossi, P., & Taglietti, V. (1995). Synaptic excitation of individual rat cerebellar granule cells in
818   situ: evidence for the role of NMDA receptors. *J Physiol, 484 (Pt 2)*, 397-413. doi:10.1113/jphysiol.1995.sp020673

819 Dudel, J., Hallermann, S., & Heckmann, M. (2000). Quartz glass pipette puller operating with a regulated oxy-hydrogen
820   burner. *Pflügers Archiv, 441*(2-3), 175-180.

821 Engel, D., & Jonas, P. (2005). Presynaptic action potential amplification by voltage-gated Na+ channels in hippocampal
822   mossy fiber boutons. *Neuron, 45*(3), 405-417. doi:10.1016/j.neuron.2004.12.048

823 Geiger, J. R., & Jonas, P. (2000). Dynamic control of presynaptic Ca2+ inflow by fast-inactivating K+ channels in
824   hippocampal mossy fiber boutons. *Neuron, 28*(3), 927-939.

825 Goldstein, S. S., & Rall, W. (1974). Changes of action potential shape and velocity for changing core conductor geometry.
826   *Biophysical journal, 14*(10), 731-757.

827 Goodman, M. B., Hall, D. H., Avery, L., & Lockery, S. R. (1998). Active Currents Regulate Sensitivity and Dynamic Range in
828   C. elegans Neurons. *Neuron, 20*(4), 763-772. doi:10.1016/S0896-6273(00)81014-4

829 Hallermann, S., De Kock, C. P., Stuart, G. J., & Kole, M. H. (2012). State and location dependence of action potential
830   metabolic cost in cortical pyramidal neurons. *Nature neuroscience, 15*(7), 1007.

831 Hallermann, S., Pawlu, C., Jonas, P., & Heckmann, M. (2003). A large pool of releasable vesicles in a cortical glutamatergic
832   synapse. *Proc Natl Acad Sci U S A, 100*(15), 8975-8980. doi:10.1073/pnas.1432836100

833 Hamill, O. P., Marty, A., Neher, E., Sakmann, B., & Sigworth, F. J. (1981). Improved patch-clamp techniques for high-
834   resolution current recording from cells and cell-free membrane patches. *Pflügers Archiv, 391*(2), 85-100.
835   doi:10.1007/BF00656997

836 Hines, M. L., & Carnevale, N. T. (1997). The NEURON simulation environment. *Neural computation, 9*(6), 1179-1209.

837 Hodgkin, A. L., & Huxley, A. F. (1952). A quantitative description of membrane current and its application to conduction
838   and excitation in nerve. *The Journal of physiology, 117*(4), 500-544. doi:10.1113/jphysiol.1952.sp004764

839 Hu, H., & Jonas, P. (2014). A supercritical density of Na(+) channels ensures fast signaling in GABAergic interneuron axons.
840   *Nat Neurosci, 17*(5), 686-693. doi:10.1038/nn.3678

841 Jayant, K., Hirtz, J. J., Jen-La Plante, I., Tsai, D. M., De Boer, W. D., Semonche, A., . . . Shepard, K. L. (2017). Targeted
842   intracellular voltage recordings from dendritic spines using quantum-dot-coated nanopipettes. *Nature*
843   *nanotechnology, 12*(4), 335.

844 Katz, B., & Miledi, R. (1967). A study of synaptic transmission in the absence of nerve impulses. *J Physiol, 192*(2), 407-436.
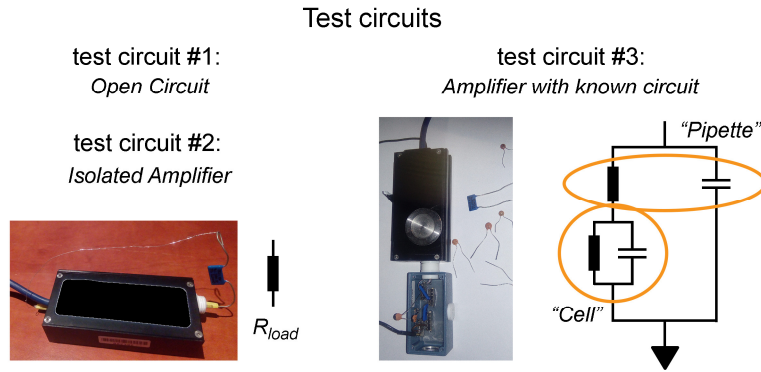845   doi:10.1113/jphysiol.1967.sp008307

846 Kawaguchi, S.-y., & Sakaba, T. (2015). Control of inhibitory synaptic outputs by low excitability of axon terminals revealed
847   by direct recording. *Neuron, 85*(6), 1273-1288.
848 Kress, G. J., Dowling, M. J., Meeks, J. P., & Mennerick, S. (2008). High threshold, proximal initiation, and slow conduction
849   velocity of action potentials in dentate granule neuron mossy fibers. *J Neurophysiol, 100*(1), 281-291.
850   doi:10.1152/jn.90295.2008
851 Kwon, T., Sakamoto, M., Peterka, D. S., & Yuste, R. (2017). Attenuation of Synaptic Potentials in Dendritic Spines. *Cell Rep,*
852   *20*(5), 1100-1110. doi:10.1016/j.celrep.2017.07.012
853 Levis, R. A., & Rae, J. L. (1993). The use of quartz patch pipettes for low noise single channel recording. *Biophysical journal,*
854   *65*(4), 1666-1677.
855 Magistretti, J., Mantegazza, M., de Curtis, M., & Wanke, E. (1998). Modalities of distortion of physiological voltage signals
856   by patch-clamp amplifiers: a modeling study. *Biophysical journal, 74*(2 Pt 1), 831-842. doi:10.1016/S0006-
857   3495(98)74007-X
858 Major, G., Larkman, A. U., Jonas, P., Sakmann, B., & Jack, J. J. (1994). Detailed passive cable models of whole-cell recorded
859   CA3 pyramidal neurons in rat hippocampal slices. *J Neurosci, 14*(8), 4613-4638.
860 Manor, Y., Koch, C., & Segev, I. (1991). Effect of geometrical irregularities on propagation delay in axonal trees. *Biophysical*
861   *journal, 60*(6), 1424-1437.
862 Martinello, K., Giacalone, E., Migliore, M., Brown, D. A., & Shah, M. M. (2019). The subthreshold-active KV 7 current
863   regulates neurotransmission by limiting spike-induced Ca 2+ influx in hippocampal mossy fiber synaptic terminals.
864   *Communications biology, 2*(1), 145.
865 Marty, A., & Neher, E. (1995). Tight-Seal Whole-Cell Recording. In B. Sakmann & E. Neher (Eds.), *Single-Channel Recording*
866   (pp. 31-52). Boston, MA: Springer US.
867 Nörenberg, A., Hu, H., Vida, I., Bartos, M., & Jonas, P. (2010). Distinct nonuniform cable properties optimize rapid and
868   efficient activation of fast-spiking GABAergic interneurons. *Proceedings of the National Academy of Sciences,*
869   *107*(2), 894-899.
870 Novak, P., Gorelik, J., Vivekananda, U., Shevchuk, A. I., Ermolyuk, Y. S., Bailey, R. J., . . . Klenerman, D. (2013). Nanoscale-
871   targeted patch-clamp recordings of functional presynaptic ion channels. *Neuron, 79*(6), 1067-1077.
872 Ogden, D., & Stanfield, P. (1994). *Patch clamp techniques for single channel and whole-cell recording.* Paper presented at
873   the Microelectrode techniques: the Plymouth workshop handbook.
874 Ohura, S., & Kamiya, H. (2018). Sodium Channel–Dependent and –Independent Mechanisms Underlying Axonal
875   Afterdepolarization at Mouse Hippocampal Mossy Fibers. *eneuro, 5*(4), ENEURO.0254-0218.2018.
876   doi:10.1523/eneuro.0254-18.2018
877 Peng, H., Bria, A., Zhou, Z., Iannello, G., & Long, F. (2014). Extensible visualization and analysis for multidimensional images
878   using Vaa3D. *Nature protocols, 9*(1), 193.
879 Peng, H., Ruan, Z., Long, F., Simpson, J. H., & Myers, E. W. (2010). V3D enables real-time 3D visualization and quantitative
880   analysis of large-scale biological image data sets. *Nature biotechnology, 28*(4), 348.
881 Peng, H., Tang, J., Xiao, H., Bria, A., Zhou, J., Butler, V., . . . Chen, J. (2014). Virtual finger boosts three-dimensional imaging
882   and microsurgery as well as terabyte volume image visualization and analysis. *Nature Communications, 5*, 4342.
883 Perkins, K. L. (2006). Cell-attached voltage-clamp and current-clamp recording and stimulation techniques in brain slices.
884   *Journal of neuroscience methods, 154*(1-2), 1-18. doi:10.1016/j.jneumeth.2006.02.010
885 Ritzau-Jost, A., Delvendahl, I., Rings, A., Byczkowicz, N., Harada, H., Shigemoto, R., . . . Hallermann, S. (2014). Ultrafast
886   Action Potentials Mediate Kilohertz Signaling at a Central Synapse. *Neuron, 84*(1), 152-163.
887   doi:10.1016/j.neuron.2014.08.036
888 Ritzau-Jost, A., Tsintsadze, T., Krueger, M., Ader, J., Bechmann, I., Eilers, J., . . . Hallermann, S. (2021). Large, Stable Spikes
889   Exhibit Differential Broadening in Excitatory and Inhibitory Neocortical Boutons. *Cell Reports, 34*(2).
890   doi:10.1016/j.celrep.2020.108612
891 Rohrbough, J., & Broadie, K. (2002). Electrophysiological analysis of synaptic transmission in central neurons of Drosophila
892   larvae. *Journal of neurophysiology, 88*(2), 847-860.
893 Rollenhagen, A., Sätzler, K., Rodríguez, E. P., Jonas, P., Frotscher, M., & Lübke, J. H. (2007). Structural determinants of
894   transmission at large hippocampal mossy fiber synapses. *Journal of Neuroscience, 27*(39), 10434-10444.
895 Roth, A., & Häusser, M. (2001). Compartmental models of rat cerebellar Purkinje cells based on simultaneous somatic and
896   dendritic patch-clamp recordings. *The Journal of physiology, 535*(2), 445-472.

897 Rowan, M. J., DelCanto, G., Jianqing, J. Y., Kamasawa, N., & Christie, J. M. (2016). Synapse-level determination of action
898   potential duration by K+ channel clustering in axons. *Neuron, 91*(2), 370-383.
899 Ruiz, A., Campanac, E., Scott, R. S., Rusakov, D. A., & Kullmann, D. M. (2010). Presynaptic GABA A receptors enhance
900   transmission and LTP induction at hippocampal mossy fiber synapses. *Nature neuroscience, 13*(4), 431.
901 Sakmann, B., & Neher, E. (1983). Geometric parameters of pipettes and membrane patches. In *Single-channel recording*
902   (pp. 37-51): Springer.
903 Schaefer, A. T., Helmstaedter, M., Sakmann, B., & Korngreen, A. (2003). Correction of Conductance Measurements in Non-
904   Space-Clamped Structures: 1. Voltage-Gated K+ Channels. *Biophysical journal, 84*(6), 3508-3528.
905   doi:10.1016/S0006-3495(03)75086-3
906 Schmidt-Hieber, C., & Bischofberger, J. (2010). Fast sodium channel gating supports localized and efficient axonal action
907   potential initiation. *Journal of Neuroscience, 30*(30), 10233-10242.
908 Schmidt-Hieber, C., Jonas, P., & Bischofberger, J. (2004). Enhanced synaptic plasticity in newly generated granule cells of
909   the adult hippocampus. *Nature, 429*(6988), 184.
910 Schmidt-Hieber, C., Jonas, P., & Bischofberger, J. (2007). Subthreshold dendritic signal processing and coincidence
911   detection in dentate gyrus granule cells. *Journal of Neuroscience, 27*(31), 8430-8441.
912 Sherman-Gold, R. (2012). *The Axon Guide, A Guide to Electrophysiology & Biophysics Laboratory Techniques* (3rd ed.):
913   Molecular Devices, LLC.
914 Sigworth, F. (1995). Electronic design of the patch clamp. In *Single-channel recording* (pp. 95-127): Springer.
915 Silver, R. A., Traynelis, S. F., & Cull-Candy, S. G. (1992). Rapid-time-course miniature and evoked excitatory currents at
916   cerebellar synapses in situ. *Nature, 355*(6356), 163-166.
917 Sivagnanam, S., Majumdar, A., Yoshimoto, K., Astakhov, V., Bandrowski, A., Martone, M. E., & Carnevale, N. T. (2013).
918   *Introducing the Neuroscience Gateway.* Paper presented at the IWSG.
919 Spruston, N., Jaffe, D. B., Williams, S. H., & Johnston, D. (1993). Voltage- and space-clamp errors associated with the
920   measurement of electrotonically remote synaptic events. *Journal of neurophysiology, 70*(2), 781-802.
921   doi:10.1152/jn.1993.70.2.781
922 Staley, K. J., Otis, T. S., & Mody, I. (1992). Membrane properties of dentate gyrus granule cells: comparison of sharp
923   microelectrode and whole-cell recordings. *Journal of neurophysiology, 67*(5), 1346-1358.
924 Strickholm, A. (1995). A single electrode voltage, current- and patch-clamp amplifier with complete stable series resistance
925   compensation. *Journal of neuroscience methods, 61*(1), 53-66. doi:10.1016/0165-0270(95)00021-L
926 Szoboszlay, M., Lőrincz, A., Lanore, F., Vervaeke, K., Silver, R. A., & Nusser, Z. (2016). Functional properties of dendritic gap
927   junctions in cerebellar Golgi cells. *Neuron, 90*(5), 1043-1056.
928 Vivekananda, U., Novak, P., Bello, O. D., Korchev, Y. E., Krishnakumar, S. S., Volynski, K. E., & Kullmann, D. M. (2017). Kv1.
929   1 channelopathy abolishes presynaptic spike width modulation by subthreshold somatic depolarization.
930   *Proceedings of the National Academy of Sciences, 114*(9), 2395-2400.
931 Wilson, C. J., & Park, M. R. (1989). Capacitance compensation and bridge balance adjustment in intracellular recording
932   from dendritic neurons. *Journal of neuroscience methods, 27*(1), 51-75. doi:10.1016/0165-0270(89)90052-6
933 Ying, L., Bruckbauer, A., Rothery, A. M., Korchev, Y. E., & Klenerman, D. (2002). Programmable Delivery of DNA through a
934   Nanopipet. *Analytical Chemistry, 74*(6), 1380-1385. doi:10.1021/ac015674m
935 Zbili, M., & Debanne, D. (2019). Past and Future of Analog-Digital Modulation of Synaptic Transmission. *Frontiers in Cellular*
936   *Neuroscience, 13*(160). doi:10.3389/fncel.2019.00160
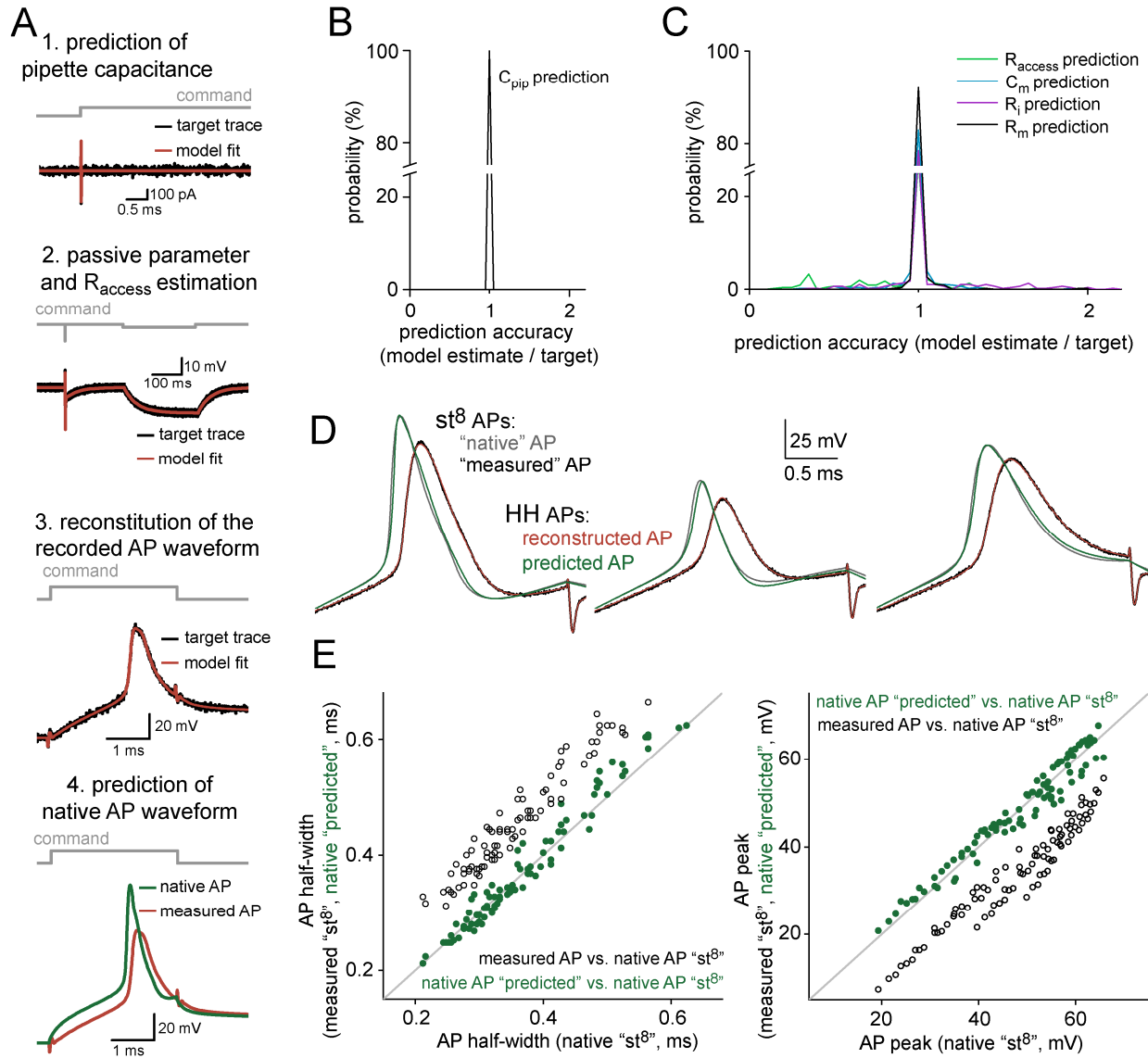
937

938

Supplementary Figure 1

Test circuits

test circuit #1:
Open Circuit

test circuit #3:
Amplifier with known circuit

test circuit #2:
Isolated Amplifier

*R*_{load}

"Pipette"

"Cell"

939

940   **Supporting data for Figures 1 and 2. Test circuits used for the characterization of the circuit components**

941

Supplementary Figure 2

942

943

Figure S2. Supporting data for Figure 4. Parameter extraction from recorded VC and CC data

944

945 (A) Outline of the consecutive optimization steps that were used to retrieve the instrumental parameters.

946 (B) Distribution of the relative error in C_{pip} estimations.

947 (C) Distribution of the relative errors present in the R_{access} and passive parameter estimations.

948 (D) Overlay of representative APs (native and measured, gray and black traces, respectively) generated using 8-state active
949 conductance models and corresponding best-fit APs generated with the standard conductances used in our final model
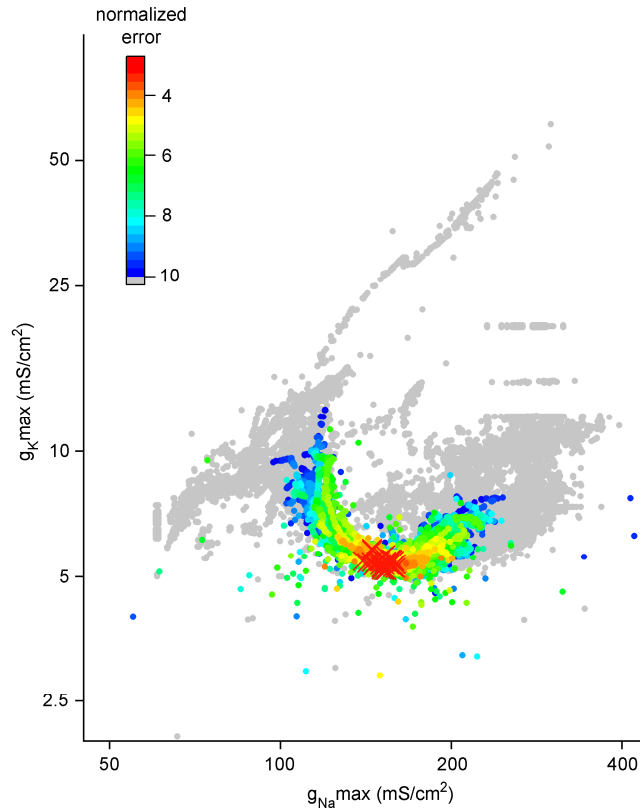950 (reconstructed and predicted, red and green traces, respectively).

951 (E) Comparison of measured AP half-width and peak values (black) and the corresponding predicted native parameters
952 (green) with the original value (n=90 simulated experiments). The line indicates equality.

953

Supplementary Figure 3

954

Supporting data for Figure 4. Uniqueness of the fit results

956 The explored parameter space during the optimization of the conductances needed to reconstruct the recorded APs (30 fitted
957 APs started from 120 initializations). Each dot represent single run during the fit (n=142605 runs). The optimization error
958 of the each run is color coded. Red crosses mark best-fit solutions.

959

Supplementary Figure 4

960
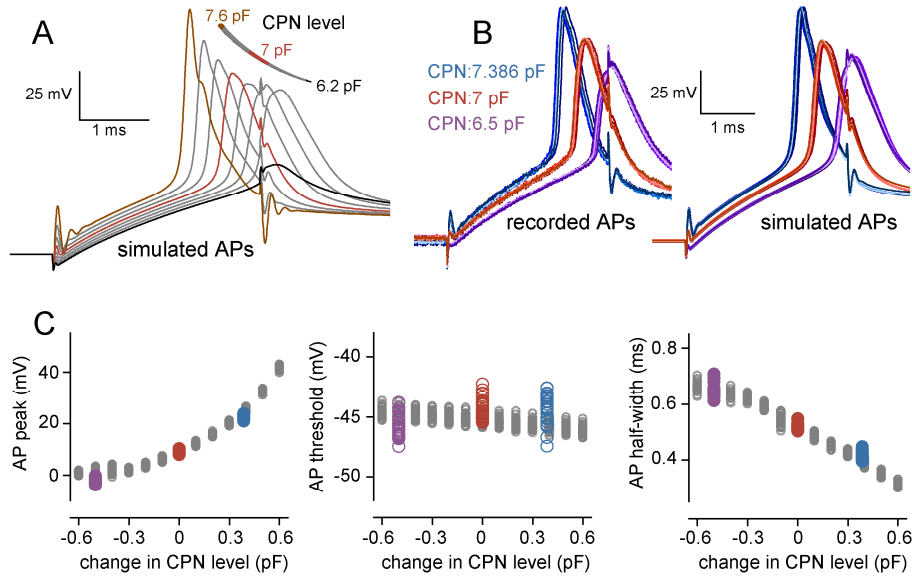
Supporting data for Figure 5. Critical influence of the applied CPN on the recorded AP waveforms

(A) Model AP waveforms simulated using the same conductance set but different CPN settings. Notice the AP failure at CPN=6.2 pF (black) and the oscillation at CPN=7.6 pF (brown).

(B) Representative APs recorded (left) and simulated (right) in the same axon with different CPN settings (n=6 APs in each CPN conditions).

(C) Effects of different CPN level on AP peak (left), threshold (middle) and half-width (right). Gray circles show the AP parameters simulated with the 30 different conductance s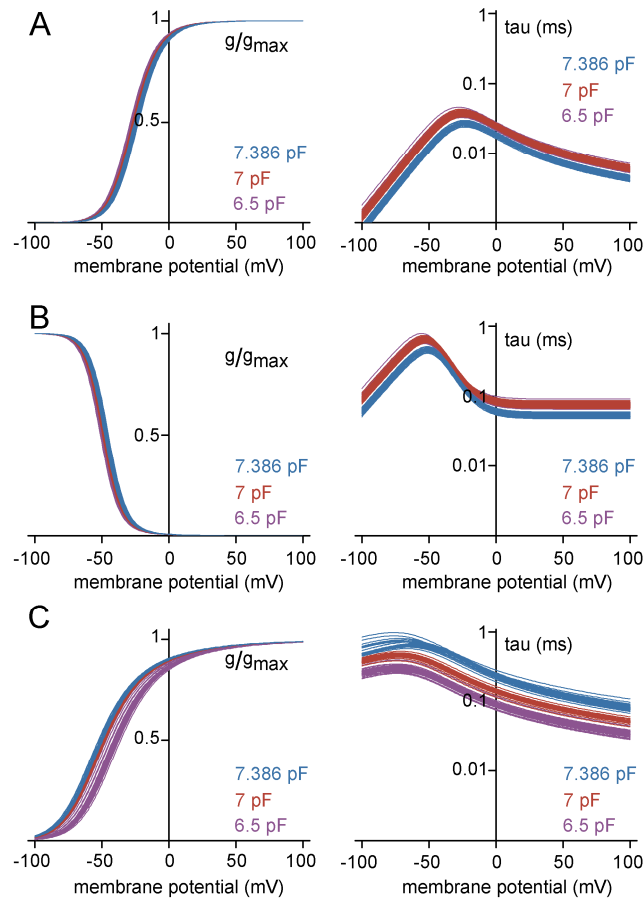ets (the same set as in Figure 4). Purple, red and blue symbols show the experimentally recorded AP parameters obtained with three different CPN settings (n=30 APs in each conditions). Zero on x-axis represents the originally set 7 pF capacitance neutralization.

Supplementary Figure 5

Supporting data for Figure 5. Gating profile of model conductances obtained from fitting of AP waveforms with different levels of distortions

(A) Voltage dependence (left) and kinetic profile (right) of the activation in Na^+ conductance models obtained by the reconstruction of the APs recorded with different CPN settings (CPN = 6.5 pF in purple, CPN = 7 pF in red and CPN = 7.386 pF in blue). Each line represent single model conductance (n=30/30/28 models).
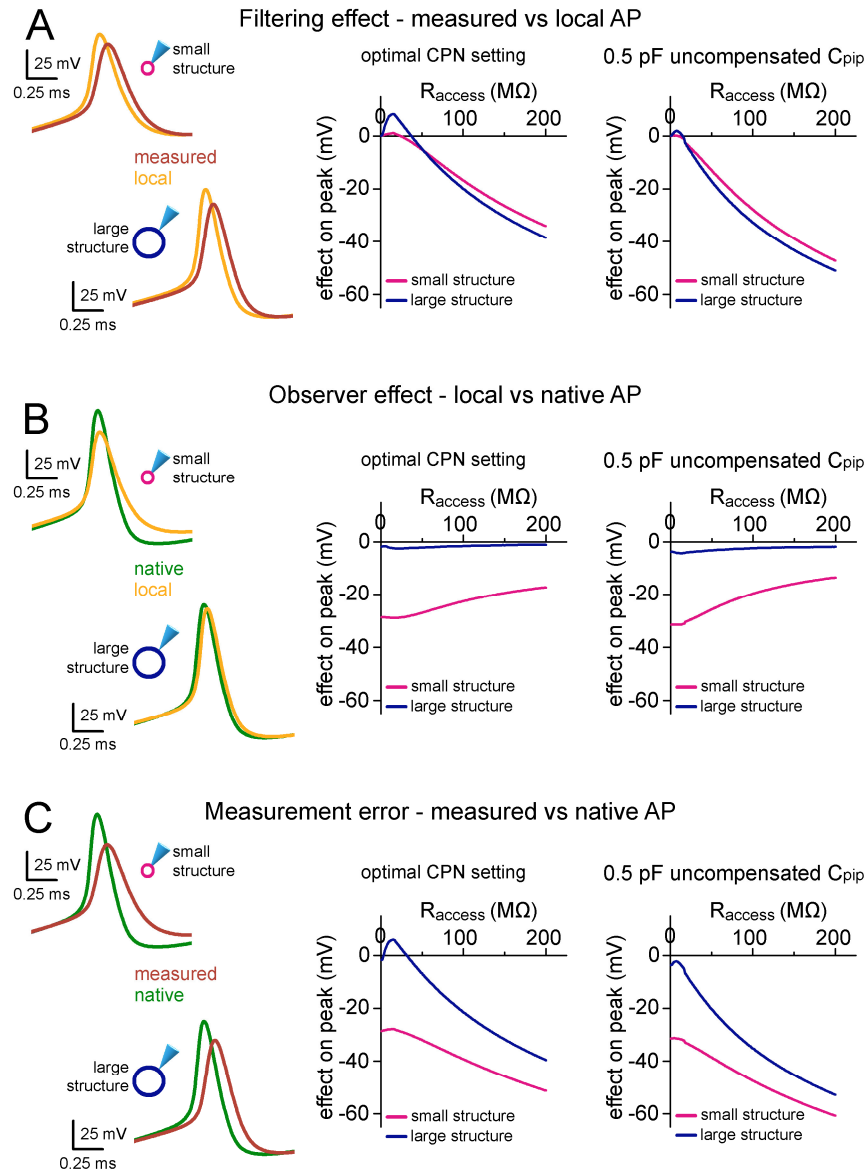
(B) Same as in panel (A) but for the inactivation of the Na^+ conductance models.

(C) Same as in panel (A) but for the K^+ conductance models

45

979

Supplementary Figure 6

980

Supporting data for Figure 7. Instrumental and structural parameters cooperatively determine signal distortions in recordings from small neuronal structures

The results of the same simulations as in Figure 7, are shown for effects on AP peak.